Title

The Dodge City Tornadoes on 24 May 2016: Damage Survey, Photogrammetric Analysis Combined with Mobile Polarimetric Radar Data

Journal

Monthly Weather Review, 146(11)

ISSN

0027-0644

Authors

Wakimoto, Roger M
Wienhoff, Zachary
Bluestein, Howard B
et al.

Publication Date

2018-11-01

DOI

10.1175/mwr-d-18-0125.1

Peer reviewed

The Dodge City Tornadoes on 24 May 2016: Damage Survey, Photogrammetric Analysis Combined with Mobile Polarimetric Radar Data

ROGER M. WAKIMOTO

Department of Atmospheric and Oceanic Sciences, University of California, Los Angeles, Los Angeles, California

ZACHARY WIENHOFF, HOWARD B. BLUESTEIN, AND DYLAN REIF

School of Meteorology, University of Oklahoma, Norman, Oklahoma

(Manuscript received 12 April 2018, in final form 11 September 2018)

ABSTRACT

Polarimetric measurements recorded by a mobile X-band radar are combined with photographs of the Dodge City, Kansas, tornado to quantitatively document the evolving debris cloud. An inner annulus or tube of high radar reflectivity encircled the tornado at low levels. A column of low cross-correlation coefficient ρ_{hv} was centered on the funnel cloud during the early stage of the tornado's life cycle. In addition, two areas of low ρ_{hv} were located near the inner annulus of high radar reflectivity and were hypothesized to be regions of high debris loading that have been reproduced in simulations of lofted debris. Another column of low ρ_{hv} was a result of strong wind speeds that were progressively lofting small debris and dust as inflow rotated around and within the weak echo notch of the hook echo. A column of negative differential reflectivity Z_{DR} was also centered on the tornado and was hypothesized to result from common debris alignment. The polarimetric structure undergoes a dramatic transition when the debris cloud was prominent and enveloped most of the funnel cloud. The weak echo column (WEC) began to fill at lower levels as large amounts of debris were lofted into the circulation. The axis of minimum ρ_{hv} shifted to a radius just beyond the funnel cloud. A column of positive Z_{DR} was collocated with the funnel surrounded by negative Z_{DR}. The negative Z_{DR} and low ρ_{hv} within the debris cloud were likely the result of some common debris alignment from wheat stems. The positive Z_{DR} within the funnel signified the presence of a few hydrometeors.

1. Introduction

Important advances in our understanding of the fine-scale structure of tornadoes have been achieved with the introduction of ground-based, mobile Doppler radars (e.g., Wurman and Gill 2000; Wurman 2002; Bluestein et al. 2004, 2007a; Lee and Wurman 2005; Kosiba and Wurman 2010; Wakimoto et al. 2011; Wurman and Kosiba 2013; Wurman et al. 2013, 2014; Kurdzo et al. 2017). More recently, these radars have been equipped with polarimetric capability that are capable of discriminating between types of hydrometeors and also identify regions characterized by lofted debris (e.g., Ryzhkov et al. 2005; Bluestein et al. 2007b, 2015; Kumjian and Ryzhkov 2008; Schultz et al. 2012a, b; Bodine et al. 2013, 2014; Snyder and Bluestein 2014; Kurdzo et al. 2015; Houser et al. 2016; Tanamachi et al. 2012; Van Den Broeke 2015; Wakimoto et al. 2015, 2016). Indeed, there have been a number of studies that have attempted to provide a detailed analysis of lofted debris within a tornado by analyzing the tornadic debris signature (TDS; Ryzhkov et al. 2005). The TDS was originally defined to be associated with radar reflectivity $Z > 45$ dBZ, cross-correlation coefficient $\rho_{hv} < 0.8$, differential reflectivity $Z_{DR} < 0.5$ dB, and collocated with an intense rotational couplet. More recent studies have proposed modification to several of these numbers suggesting that defining precise threshold values demarcating a TDS is challenging (e.g., Kumjian and Ryzhkov 2008; Bodine et al. 2013, 2014; Van Den Broeke and Jauernic 2014). There is general agreement that ρ_{hv} provides a better indicator of lofted debris within a tornado than Z_{DR} since the latter exhibits a positive bias when rain is present (Bluestein et al. 2007b) and a negative bias when there is Mie

Denotes content that is immediately available upon publication as open access.

Corresponding author: Roger M. Wakimoto, wakimotoroger@gmail.com

DOI: 10.1175/MWR-D-18-0125.1

scattering and/or common debris alignment (Ryzhkov et al. 2005; Bluestein et al. 2007b; Cheong et al. 2017; Umeyama et al. 2018). Anomalously low values of Z_{DR} can also be due to differential attenuation if located downrange of a heavy precipitation core (Schultz et al. 2012a).

It is well known that lofted debris will impact both the observed Doppler velocities and the tornado's wind field. Bodine et al. (2016a) simulated the impact of wood boards on the measured velocities in tornadoes. At S band, the boards are the dominant scatterers except when the wood board concentrations are very low. In contrast, raindrops are the dominant scatterers at Ka and W bands. At intermediate frequencies, (e.g., X band), the air and simulated Doppler velocity difference exhibited large variability depending on the relative concentrations of raindrops and wood boards. The authors cautioned that their results are for only one debris type.

Strong centrifuging of hydrometeors and debris within a tornado resulting in a positive bias in radial velocities relative to the airspeed has been reported by several investigators (e.g., Dowell et al. 2005; Wakimoto et al. 2012; Nolan 2013; Bodine et al. 2014). The bias can have a nontrivial impact on the derived vertical velocities (e.g., Wakimoto et al. 2012; Nolan 2013; Bodine et al. 2016a) and also contribute to the absence of prominent convergent flow at low levels, except in a few cases (e.g., Wurman et al. 2007, see their Fig. 3; Kosiba and Wurman 2013), even though convergence has been documented in numerical simulations and laboratory experiments of intense vortices. Lewellen et al. (2008) using a large-eddy simulation model documented reductions in azimuthal velocities of 20%–50% when lofted debris (sand particles) was included. Bodine et al. (2016b) found that sand particles could cause reduction in surface wind speeds up to 50%. Although the peak wind velocities are reduced with the addition of lofted debris, this does not necessarily mean that the damage potential is reduced. Total swirl momentum including the effects of debris can increase and ''sandblasting'' can combine to produce even greater damage (Lewellen et al. 2008) and can contribute to the observed damage along the tornado track (e.g., Doswell and Brooks 2002).

Lofted debris can be visually apparent as a debris cloud that envelops the funnel and is a characteristic feature of many tornadoes. The size and shape of the cloud is dependent on the tornadic wind speeds but also the type of debris that is lofted (e.g., Lewellen et al. 2008). Although there have been numerous photographs and movies of debris clouds documented in the literature and an increasing number of cases when polarimetric data were collected by radars, there has not been an attempt to combine detailed photogrammetric analysis of debris

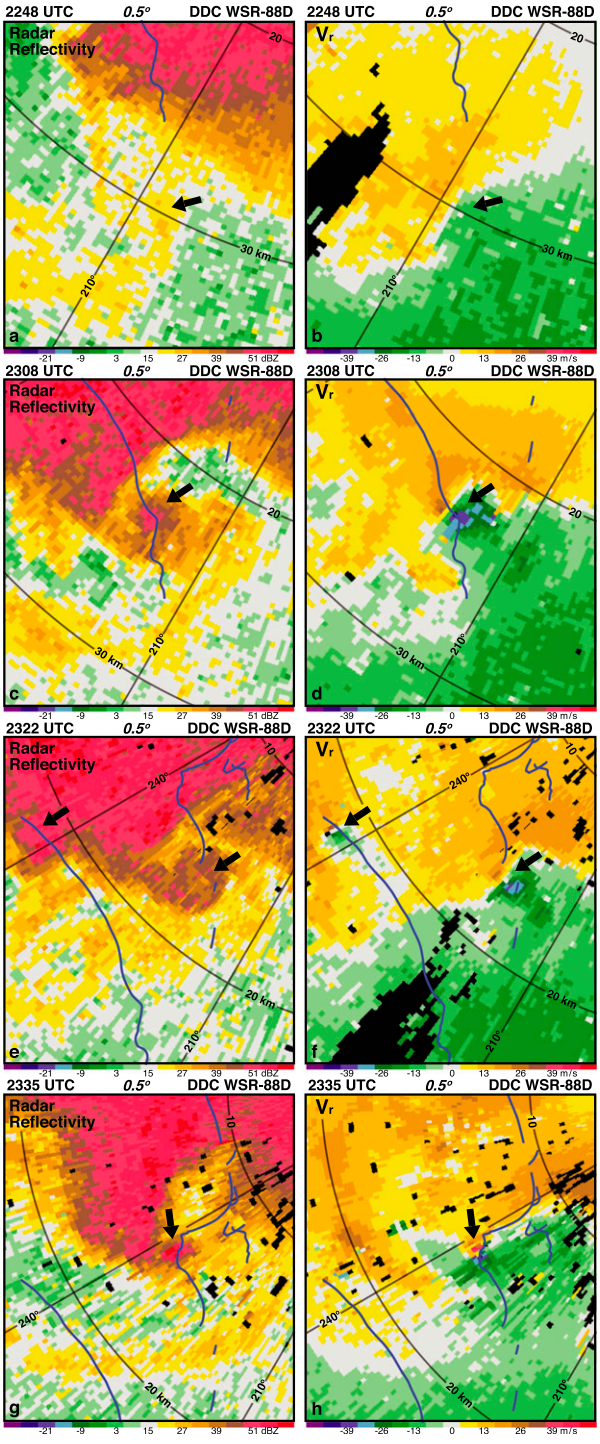

FIG. 1. Radar images at 0.5° elevation angle from the Dodge City (DDC) WSR-88D. (a) Radar reflectivity and (b) Doppler velocity at 2248 UTC. (c) Radar reflectivity and (d) Doppler velocity at 2308 UTC. (e) Radar reflectivity and (f) Doppler velocity at 2322 UTC. (g) Radar reflectivity and (h) Doppler velocity at 2335 UTC. Blue lines represent the location of tornado tracks that are enlarged in Fig. 2. Black arrows denote the location of shear features or rotational couplets in Doppler velocity and enhanced reflectivity within the hook echo.

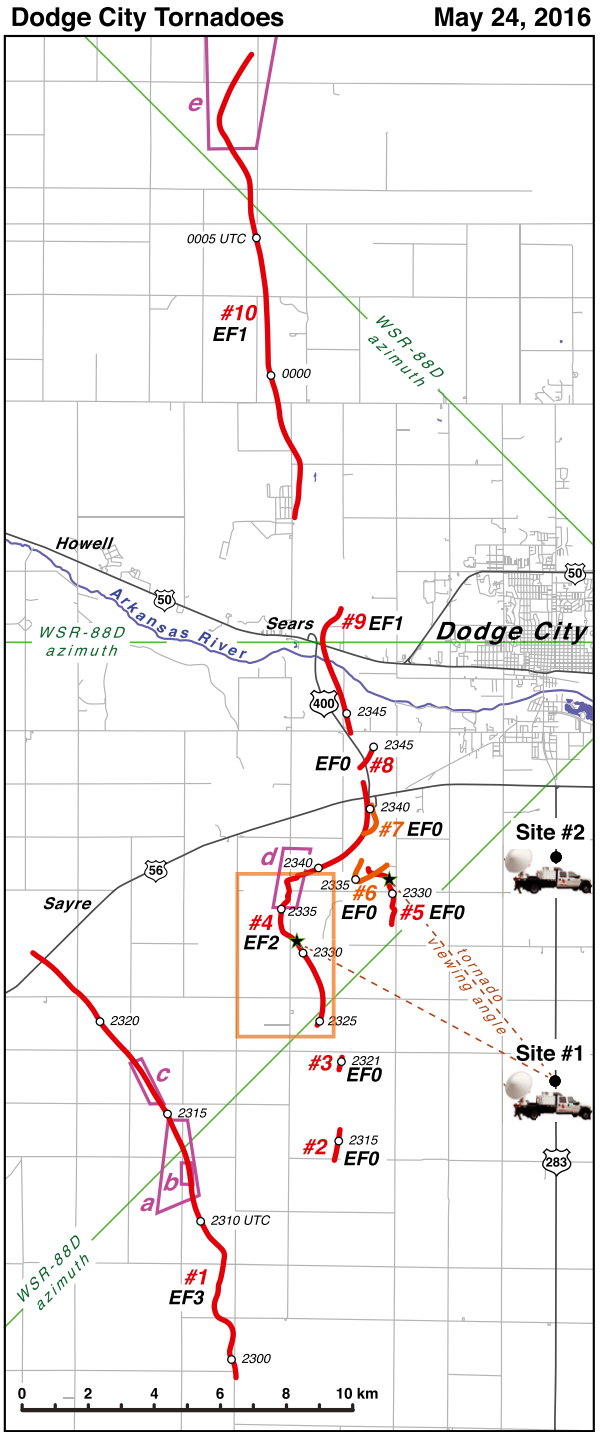

FIG. 2. Damage map of the Dodge City, KS, tornadoes on 24 May 2016. Red lines represent the tornado tracks with the locations of the tornado labeled at select times. EF ratings are shown for each tornado. Black dots represent two deployment locations of the RaXPol mobile Doppler radar (shown by an icon of the truck). Photographs and videos of the tornado were taken at both sites. Green lines represent the viewing angles from the Dodge City WSR-88D (DDC). Areas enclosed by the magenta lines represent aerial photographs shown in Fig. 3. Black stars represent the locations of the two tornadoes shown in Fig. 4. Brown dashed lines represent the viewing angles from site 1. The area enclosed by the brown box is enlarged in Fig. 5.

clouds accompanying a tornado with polarimetric radar data. Van Den Broeke (2015) examined TDS variability and debris fallout signatures for a number of tornadoes but no visual information was presented. In addition, the coarser resolution data collected by the WSR-88Ds were used in his study. Wakimoto et al. (2015) merged polarimetric data with images of the 31 May 2013 El Reno, Oklahoma, tornado. A prominent and large TDS was associated with the tornado but the debris cloud documented in the photographs was obscured by poor visibility and precipitation. Qualitative photogrammetric analysis of a tornado was performed by Bluestein et al. (2007b). Their results showed general agreement between the dust/debris cloud and the regions of low Z_{DR} and ρ_{hv} within the TDS. Bluestein et al. (2007b) did not attempt to merge the polarimetric data with images of the tornado and the radar data were also restricted to lower levels so that variations of Z_{DR}, ρ_{hv}, and radar reflectivity data could not be examined as a function of height with the photographs. Griffin et al. (2017) presented the three-dimensional wind field of a TDS associated with an intense tornado; however, no visual information was provided. It would be important and valuable to be able to merge collocated visual and radar observations of a tornado. To date, observational studies of lofted debris have largely focused on radar polarimetric measurements with little documentation of the visual characteristics of the debris cloud and its relationship to the funnel.

On 24 May 2016, a series of supercells formed over western Kansas and produced a number of tornadoes. Wienhoff et al. (2018) have examined radar data collected on this day and produced dual-Doppler analyses of some of the tornadoes mentioned in this paper. One cell west of Dodge City, Kansas, was intercepted by the mobile rapid-scanning X-band polarimetric Doppler radar (RaXPol; Pazmany et al. 2013) as it produced several tornadoes while the visual characteristics of the condensation funnel and debris cloud were recorded by a high-resolution camera. The views of the tornado and the lofted debris were largely unimpeded by precipitation and poor visibility. The tornadoes moved slowly which resulted in continuous volume scans of radar data being collected over an extended period. In this paper, radar reflectivity, single-Doppler velocities, Z_{DR}, and ρ_{hv} data

are combined with the photographs in order to relate these measurements to the visual characteristics of the lofted debris. Section 2 discusses RaXPol, photogrammetric techniques used in this study and the damage survey. A series of vertical cross sections that combine polarimetric data with photos taken of the tornado are shown in section 3. A discussion and summary are presented in section 4.

2. RaXpol, photogrammetry, and the damage survey

The primary observational platform used for the current study is RaXPol. The radar transmits at a wavelength of 3.1 cm, the antenna diameter is 2.4 m, and the 3 dB (half power) beamwidth is 1°. The antenna rotates as rapidly as 180° s^{-1}. The range resolution is 30 m, oversampled such that the range gates were 15 m. The frequency-diversity technique (e.g., Hildebrand and Moore 1990) was used to increase the number of independent samples needed to calculate the radar parameters while in rapid scan mode. The elevation angles within an individual volume scan were generally from 0° to 6° in 1° steps and each volume was completed in ~20 s. The time period of primary data collection for photogrammetric analyses occurred during 2324–2335 UTC (UTC = CDT+ 5 h) capturing the evolution of the debris cloud and its relationship with the tornado. The interested reader is referred to Pazmany et al. (2013) for additional information on RaXPol.

A number of investigators have used photogrammetry to quantitatively analyze pictures of a condensation funnel or a cloud field (e.g., Malkus 1952; Bluestein 1986; Wakimoto and Martner 1992; Zehnder et al. 2007). Photogrammetry requires knowledge of the precise location of the photographer and the azimuth angles of targets than can be identified on the picture horizon. The azimuth angles to known targets are necessary in order to calculate the tilt angle and the effective focal length using spherical trigonometry. Subsequently, an azimuth- and elevation-angle grid can be created and superimposed onto the photograph. A comparison of the azimuth angles of the targets visible on the horizon of the picture with the calculated azimuth-angle grid reveal that the angle errors range between 0.1° and 0.2° (17–34 m during the analysis times when the tornado is farthest from the radar). The photogrammetrically derived angle grid is equivalent to the radar scanning angles if the photographs are taken close to the radar antenna as was the case for the current study. The tornado motion was taken into account by shifting the radar data; however, this correction was small because the radar volume scans were completed in ~20 s. The time of the photograph was used as the analysis time. An overview of photogrammetry can be found in Abrams (1952) and Holle (1986).

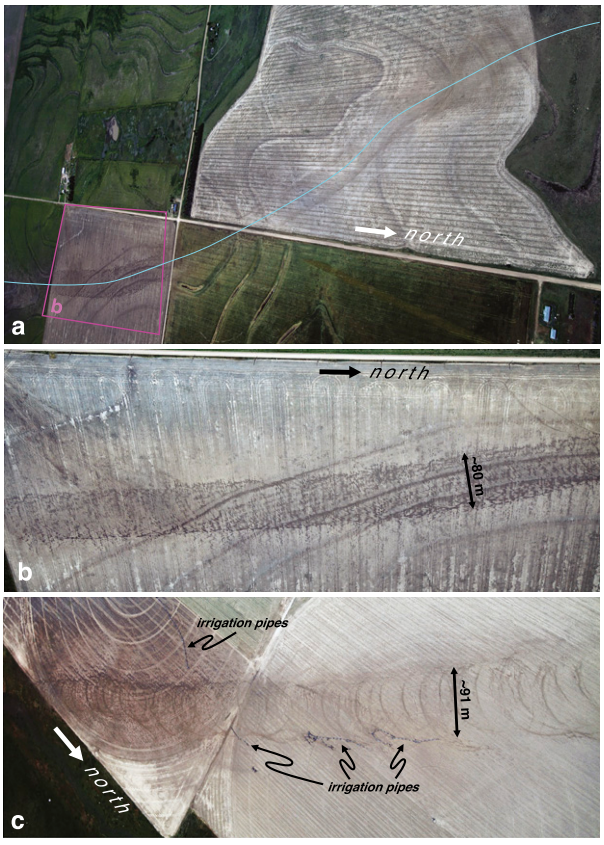

FIG. 3. (a)–(e) Aerial photographs of the Dodge City tornadoes. Locations of the photographs are shown by the letter identifiers plotted in Fig. 2. The area enclosed in (b) is highlighted by the magenta lines in (a). Locations of the tornado tracks are shown by the light blue lines in (a), (d), and (e). Tornado swath marks are also highlighted in (d). The approximate widths of the tornado are shown in (b) and (c).

The relationship between the damage paths of the Dodge City tornadoes and four times recorded by the Dodge City WSR-88D (DDC) is shown in Fig. 1. A shear zone is apparent in the Doppler velocity field at 2248 UTC (black arrow in Fig. 1b) approximately 12 min before the first tornado developed. A circular region of radar reflectivity can be identified in Fig. 1a (black arrow) denoting the incipient stages of the hook echo. A pronounced hook echo with radar reflectivities greater than 50 dBZ and a rotational couplet (black arrows in Figs. 1c and 1d, respectively) are centered on the tornado 1 (Fig. 2) track at 2308 UTC. The strong echoes are also collocated with relatively low ρ_{hv} (not shown) indicative of lofted debris. The DDC echo and velocity scans at 2322 UTC were recorded before the dissipation of tornado 1 and the formation of tornado 4 (Fig. 2). The black arrows denote

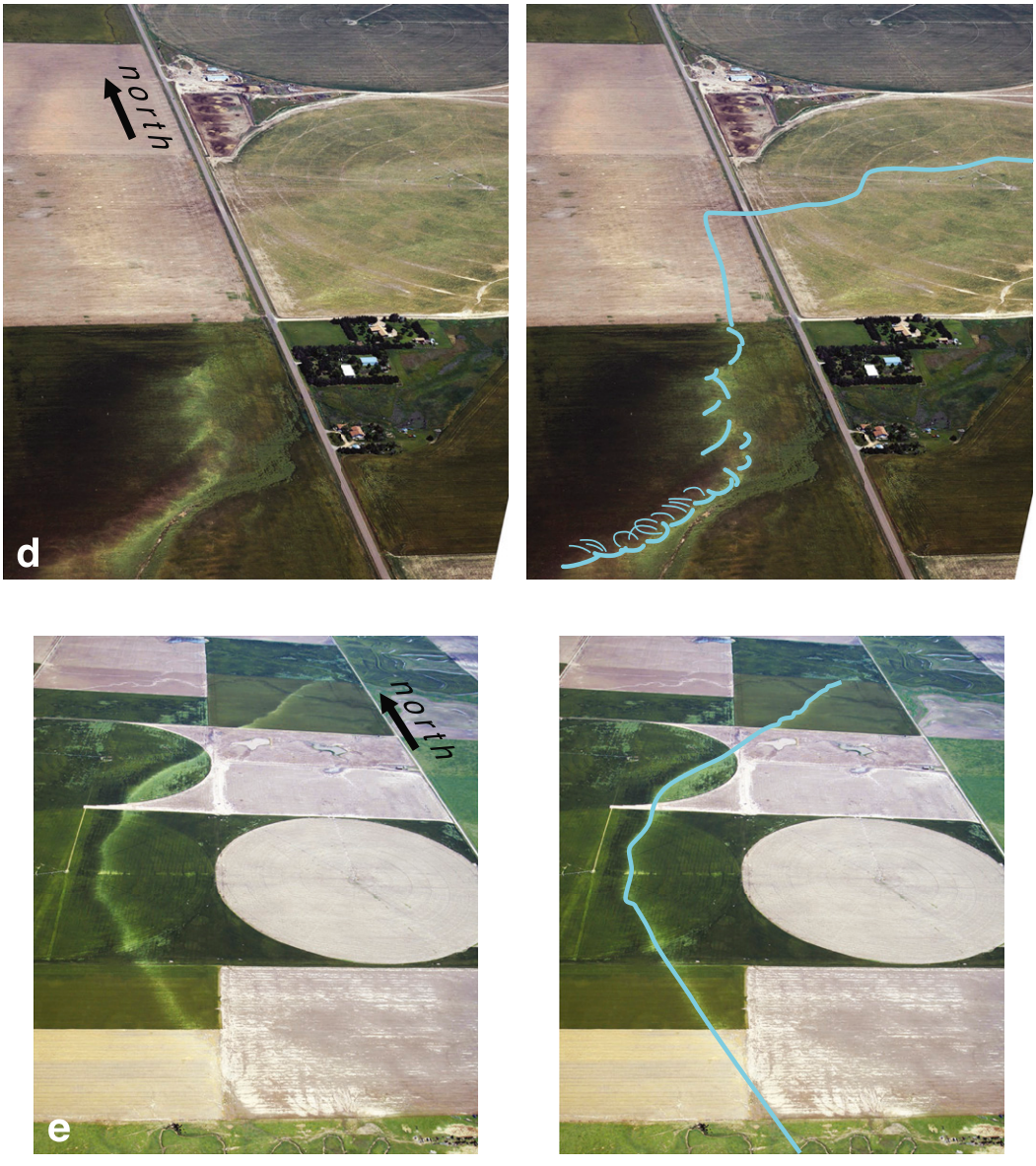

FIG. 3. (*Continued*)

the location of the two rotational couplets and hook echo appendages (Figs. 1e and 1f) that were identifiable at this time. Tornado 4 was located in the middle of its damage track at 2335 UTC (Figs. 1g and h). A smaller but stronger rotational couplet is evident and it is accompanied by an enhanced region of radar reflectivity similar to the images shown in Figs. 1c and 1d. The radar images depicted at 2335 UTC are close to the times that photogrammetric analysis of tornado 4 was performed (section 3).

A detailed aerial damage survey using a Cessna aircraft, performed on 27 May, identified 10 tornadoes over the area west of Dodge City (Fig. 2). The EF rating of each tornado is shown in the figure. All of the tornadoes depicted in the figure were scanned by RaXPol while it was deployed at sites 1 (2313–2346 UTC) and 2 (2356–0006 UTC). The tornado tracks shown on the figure were reconstructed based on damage swath marks in the ground (Fig. 3) and the rotational couplet identified in the Doppler velocities. The first tornado formed at ~2300 UTC, ~20 km south southwest of Dodge City (Fig. 2). The subsequent tornadoes tracked in a general northward direction with the last tornado dissipating at ~0010 UTC. Fortunately, the tornadoes occurred in rural areas and impacted few structures as shown in Figs. 2 and 3. The location and surface width of tornado 1 were well defined at several locations along its track

(Figs. 3a–c). Approximate dimensions of the tornado width are noted in Figs. 3b and 3c. Aerial photographs reveal a prominent ''right turn'' by tornado 4 (Figs. 2 and 3d) and a distinct lineation mark at the end of the tornado 10 track (Figs. 2 and 3e).

The tornado tracks and times plotted in Fig. 2 reveal that there were several instances when multiple tornadoes could be visually identified. Two tornadoes were photographed at 2330:50 UTC (Fig. 4a) from site 1. The stars plotted in Fig. 2 denote the location of the two tornadoes at the time that the photograph was taken. Both tornadoes are pendant from a prominent wall cloud that is associated with a sloping cloud base. The high-resolution scans recorded by RaXPol at 2330:51 UTC are shown in Figs. 4b and 4c. A well-defined weak echo hole (WEH) or minimum in radar reflectivity surrounded by a high reflectivity tube (e.g., Fujita 1981; Wurman et al. 1996; Wakimoto et al. 1996; Wurman and Gill 2000; Dowell et al. 2005) denotes the location of tornado 4 (Fig. 4b). The WEH develops in response to centrifuging of hydrometeors and debris within an intensifying circulation. A rotational couplet is centered on the WEH (Fig. 4c). A smaller and weaker couplet associated with tornado 5 is also highlighted in Fig. 4c. The size and intensity of the couplet is not surprising owing to the narrowness of the funnel depicted in the photograph (Fig. 4a). There is no obvious distinguishing echo appendage accompanying tornado 5 (Fig. 4b).

The focus of the current study is the photogrammetric analysis of tornado 4 in the region depicted in Fig. 5. The tornado track based on the aerial survey and the rotational couplet locations and times are shown in the figure. Also plotted in the figure are the locations of the tornado during the analysis times presented in section 3. The finescale analyses include tornadogenesis, the formation of the funnel cloud, and the debris cloud enveloping the condensation funnel. Fortunately, the aerial survey provided the most up-to-date information regarding land cover at the time the tornado traversed the terrain. All sectors along the tornado path have been labeled with the land-cover type (Fig. 5) that alternated between wheat and exposed dirt fields (e.g., Fig. 3d).

3. RaXPol low-level scans and vertical cross sections through the tornado

RaXPol recorded high temporal and spatial data of radar reflectivity, Doppler velocity, Z_{DR}, and ρ_{hv} that could be quantitatively compared with the visual characteristics of tornado 4. The unique aspects of the current study are the large number of consecutive radar scanning volumes that can be integrated into a photogrammetric analysis and the detailed comparison of the evolving funnel and debris cloud with the polarimetric data. The range to the rotational couplet (i.e., the tornado) was determined using single-Doppler velocity data from RaXPol. This range was used to construct pseudovertical cross sections through the weak echo column (WEC; Tanamachi et al. 2012) and the rotational couplet using the raw data collected by the radar. The use of raw rather than interpolated data results in a finescale analysis of the radar fields. These cross sections are along curved surfaces since a constant range is used. The distance from RaXPol to the tornado varied for each analysis time. Accordingly, the pictures presented in this section were enlarged or reduced so that the length scale valid at the distance to the tornado was the same. This adjustment facilitates the comparison between the profiles (e.g., changes in the funnel cloud identified in the photos are not a result of different ranges to the tornado).

The polarimetric variables could contain statistical errors in areas of low signal-to-noise ratios such as the WEC. These errors could lead to large spatial variability of the raw plotted fields and sensitivity to the location of the vertical cross section. This topic is discussed in the appendix.

a. 2324:45–2324:57 UTC

Tornadogenesis is defined as the time when damage was documented at the ground (Fig. 5). The radar reflectivity, single-Doppler velocities, and polarimetic data recorded by the low-level RaXPol scan at 2324:46 UTC is shown in Fig. 6. The hook echo is evident as a band of high radar reflectivity coiled up around a WEH (Fig. 6). A rotational couplet is apparent but not intense and low ρ_{hv} and Z_{DR} are centered at the location of the WEH (Fig. 6). The incipient stages of a funnel cloud can be seen pendant from cloud base at 2324:44 UTC (Fig. 7a). The WEC was subjectively defined as radar reflectivities <20 dBZ and is highlighted by the shaded region in Fig. 7b. The WEC is centered on the funnel cloud aloft with minimum radar reflectivities <10 dBZ. The band of high radar reflectivity that connects the hook echo with the main body of the storm (Fig. 6) is apparent as the tilted column of echoes >40 dBZ located to the south (left) of the funnel cloud. The WEC is approximately centered within the velocity couplet (Fig. 7c). The maximum receding velocities and a minimum approaching velocities are >30 and <-30 m s^{-1}, respectively. The maximum azimuthal shear is ~ 0.5 s^{-1}. The location of the lofted debris is depicted by the vertical profile of ρ_{hv} (Figs. 7c and 7f). Shaded regions that denote low ρ_{hv} areas less than 0.40 are embedded within the WEC suggesting that the particles are small owing to the low radar reflectivity. Ryzhkov et al. (2005) and Kumjian and Ryzhkov (2008) have noted similar low radar reflectivity and ρ_{hv} characteristics in inflow

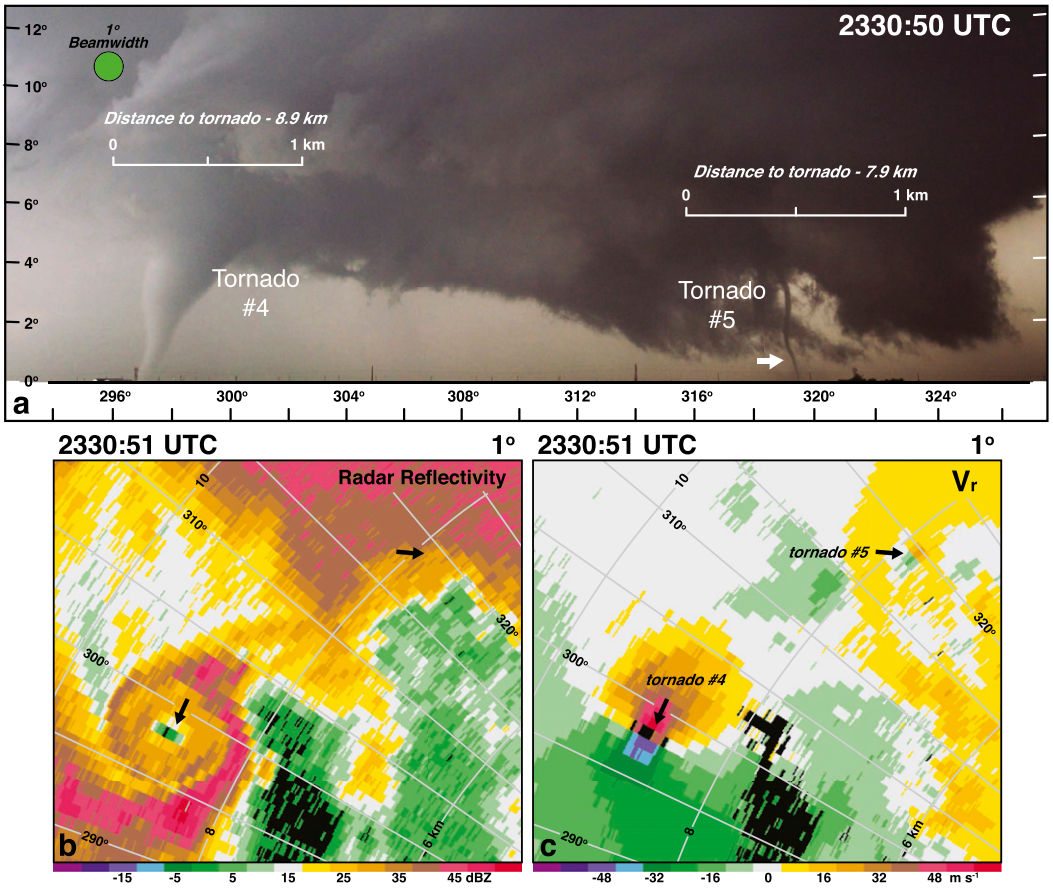

FIG. 4. (a) Photograph of tornadoes 4 and 5 at 2330:50 UTC taken at site 1. The two length scales are valid at the distance of the two respective tornadoes. The location of the tornadoes at 2330:50 UTC is shown by the black stars in Fig. 2. (b) Radar reflectivity image at 1° elevation angle recorded by RaXPol at 2330:51 UTC. (c) Doppler velocity image at 1° elevation angle recorded by RaXPol at 2330:51 UTC. Black arrows denote the locations of a weak echo hole within the hook echo and the rotational couplets in (b) and (c), respectively.

regions of supercells that were attributed to lofted light debris. Past studies have shown that dust is highly diverse in shape and aspherical, which would lead to low ρ_{hv} (e.g., Okada et al. 2001; Kandler et al. 2007).

The column of low ρ_{hv} extending into cloud base is surprising since tornado formation has just occurred and no visible debris can be identified in the photo. However, low ρ_{hv} signatures indicative of a TDS have been previously documented prior to tornadogenesis (e.g., Saari et al. 2014; Van Den Broeke 2015). They hypothesize that debris is lofted as the wind field strengthens prior to tornadogenesis. The tornado developed over a wheat field in the current study (Fig. 5) where small particles or sparse debris, not visually identifiable in these photographs, could have been lofted by an intensifying circulation. The pixel resolution of the photographs at a distance of 9 km (average distance to the tornado) is ~0.5 m. Sparse debris much less than this dimension would not be visibly resolvable in the images. Debris fallout from the dissipation of tornado 3 that was subsequently entrained by tornado 4 may have also been a contributing factor as proposed by Houser et al. (2016). Indeed, a TDS could be continuously tracked between the demise and genesis of tornadoes 3 and 4, respectively. In addition, the short track of tornado 3 passed over a wheat field (not shown) where wheat stems may have been lofted in the circulation.

The cross section of differential reflectivity (Fig. 7e) reveals negative Z_{DR} (<-2 dB) within the WEC and low ρ_{hv}. Common debris alignment (Ryzhkov et al. 2005; Bluestein et al. 2007b) may be contributing to the negative Z_{DR} observed in the present case (i.e., vertically oriented debris). Bodine et al. (2014) proposed that given the wide range of scatterer characteristics within a resolution volume, some degree of common scatterer alignment could produce negative Z_{DR} even when ρ_{hv} is low. It is possible that wheat stems were lofted by the tornado in this study and are exhibiting some common

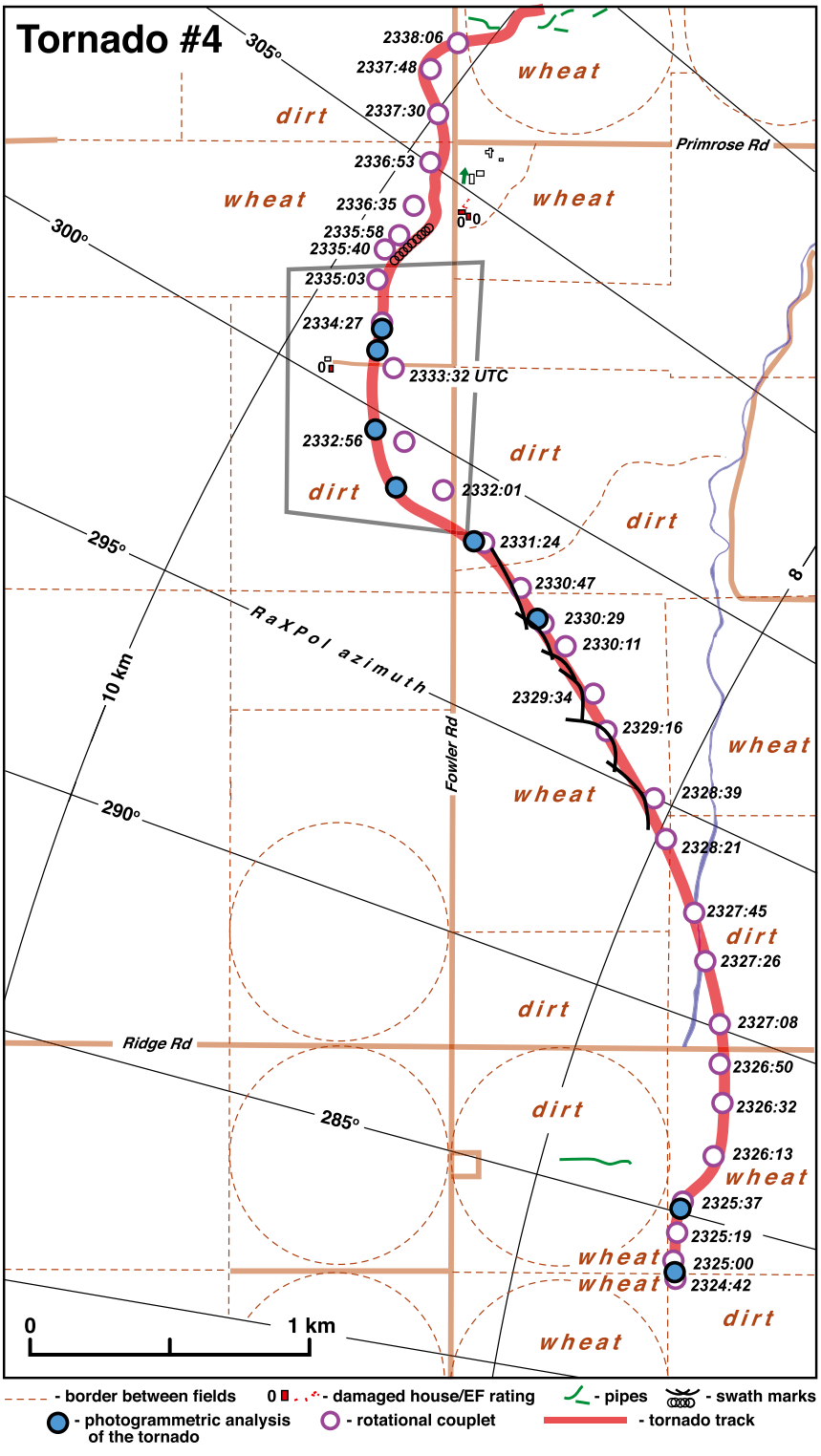

FIG. 5. Enlargement of damage track of tornado 4. Symbols plotted in the figure are shown in the legend. White circles denote the locations of the rotational couplet and were determined using RaXPol scans at 0° elevation angle. The blue circles represent the locations of the tornado during the analysis times discussed in section 3. The characteristics of the land surface traversed by the tornado are labeled on the figure. Azimuth and range from RaXPol site 1 are plotted. Gray box is enlarged in Fig. 18. The area enclosed by this figure is shown by the brown box in Fig. 2.

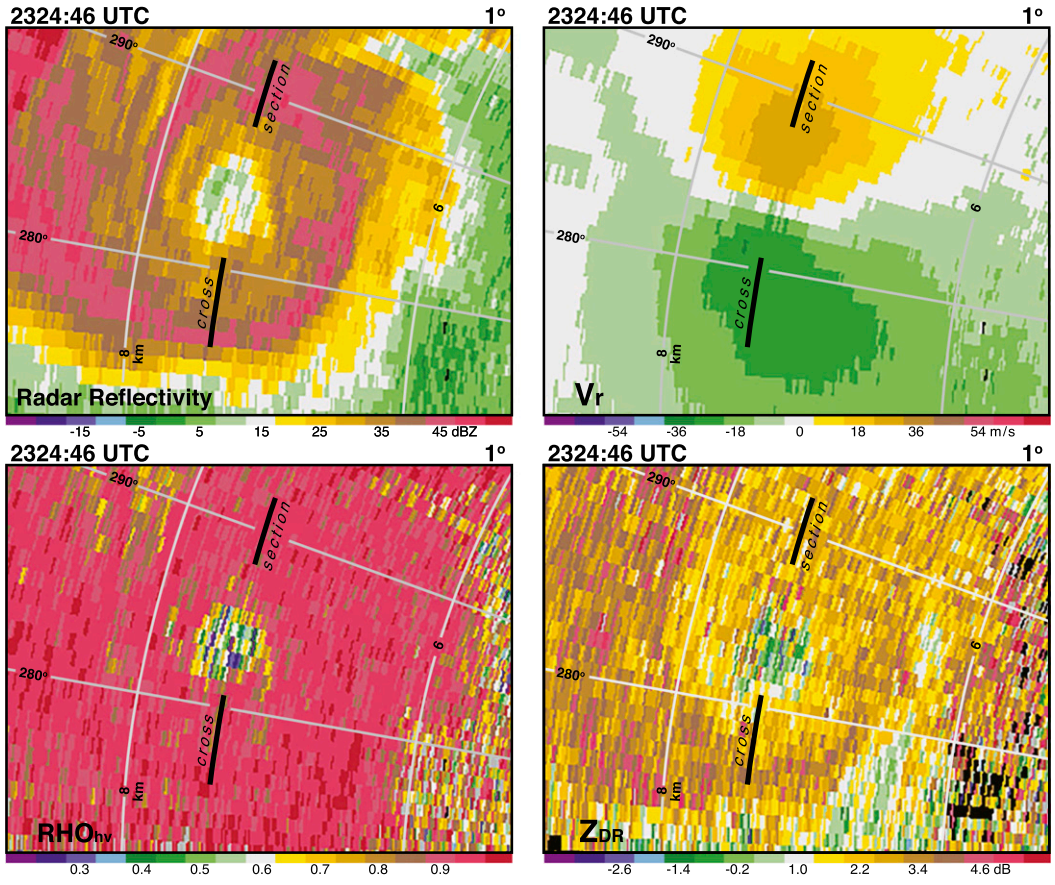

FIG. 6. Radar reflectivity, single-Doppler velocities V_r, cross-correlation coefficient ρ_{hv}, and differential radar reflectivity Z_{DR} scans from RaXPol at 1° elevation angle at 2324:46 UTC. Range and azimuth angle grid is shown by the gray lines. Black line represents the location of the cross section shown in Fig. 7.

debris alignment. Light debris such as wheat stems may not be reflective or could be present in low concentrations, which may explain the low radar reflectivity. However, Mie or resonance scattering could be occurring in one scattering direction. Differential attenuation may also be contributing to the negative Z_{DR}. Cheong et al. (2017) and Umeyama et al. (2018) used a numerical polarimetric radar emulator to hypothesize that common alignment of lofted debris composed of leaves may occur because of centrifuging effects. The band of high reflectivity noted in Figs. 7b and 7f is associated with $Z_{DR} > 3$ dB, which is indicative of large raindrops. The high Z_{DR} encircling the developing tornado can also be identified in Fig. 6 (also documented by Griffin et al. 2017). This band may be an extension of the Z_{DR} arc (e.g., Kumjian and Ryzhkov 2008, 2009) based on the radar images recorded by RaXPol.

b. 2325:41–2325:51 UTC

The funnel cloud extends approximately halfway between cloud base and the surface at 2325:35 UTC (Fig. 8a). The minimum radar reflectivities are less than 0 dBZ within the WEC (Fig. 8b) as the rotational couplet intensifies and is accompanied by a smaller radius of maximum of winds (Fig. 8c). It is noteworthy that only 1 min has elapsed between these radar volumes illustrating the rapid centrifuging of hydrometeors that contribute to weaker echoes within the WEC [rapid centrifuging was also noted by Wakimoto et al. (2011)]. The region of radar reflectivity <0 dBZ extends from cloud base to near the surface. The minimum radar reflectivity does not extend to the ground where the strongest centrifuging of particles would be expected to occur. This is likely a result of small debris that is lofted at low levels and is not visible in the photograph (Fig. 8a). The ρ_{hv} shown in Figs. 8d and 8f continues to fall with the minimum (<0.20) located within 250 m above ground level (AGL; hereafter all heights are AGL). The minimum ρ_{hv} near the surface supports the presence of low-level lofted debris (Fig. 8f). Wakimoto et al. (2011) proposed a similar scenario during the formative stages of the LaGrange

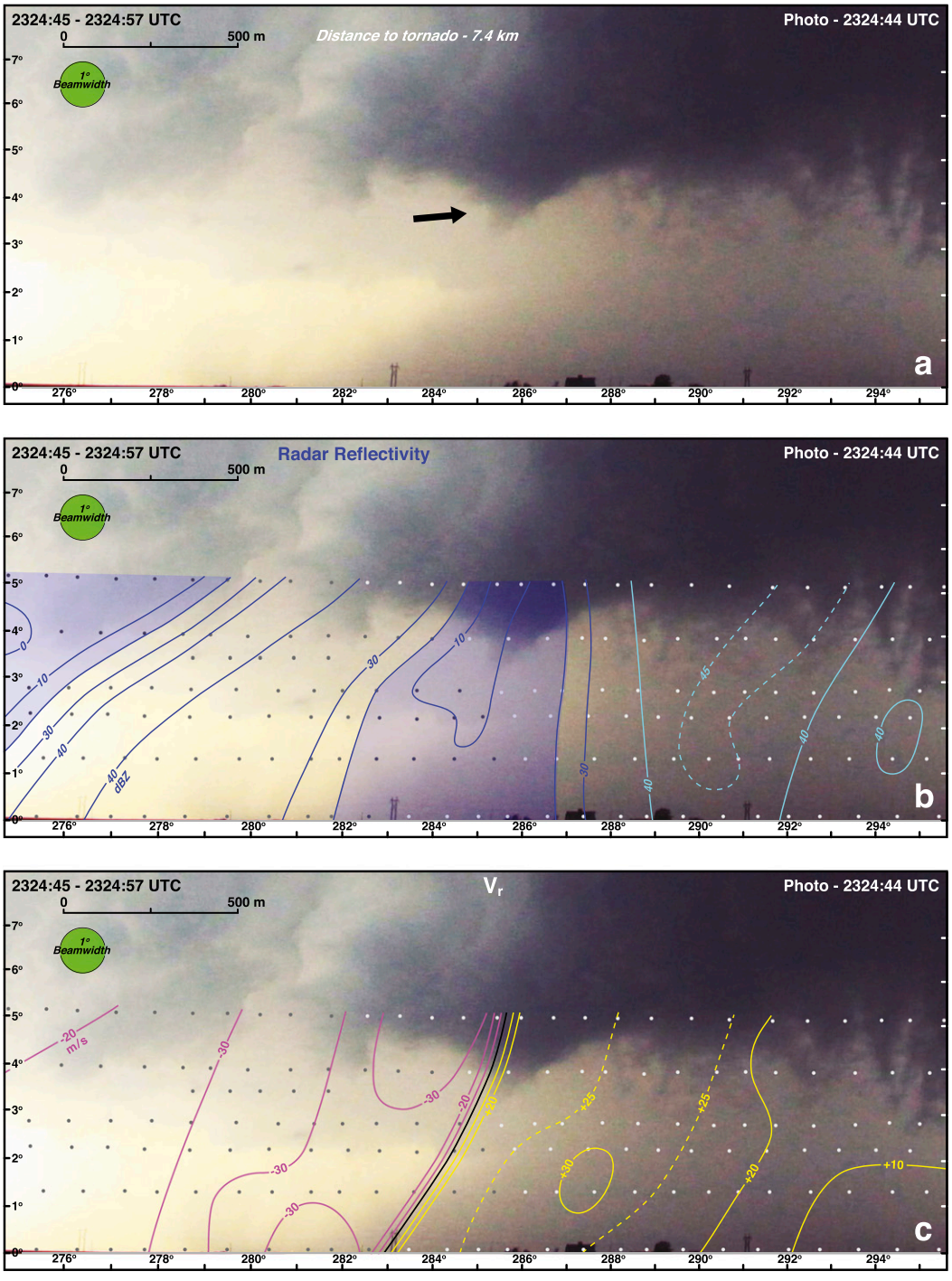

FIG. 7. (a) Photograph of Dodge City tornado 4 at 2324:44 UTC. Radar volume scan is 2324:45–2324:57 UTC. (b) Radar reflectivity (dBZ). Values < 20 dBZ are shaded light blue. (c) Ground-relative single-Doppler velocities (m s^{-1}). Magenta and yellow lines are isopleths of approaching and receding single-Doppler velocities, respectively. (d) Cross-correlation coefficient ρ_{hv}. Values < 0.40 are shaded red. (e) Differential reflectivity Z_{DR}. Red and green lines are isopleths of negative and positive Z_{DR}, respectively; $Z_{DR} > 3$ dB are shaded green. (f) Radar reflectivity and ρ_{hv}. The green circle represents the 1° beamwidth of the radar. The scales labeled on the figures are valid at the distance to the center of the tornado. The small dots represent the raw data points from RaXPol. Black arrow in (a) denotes the location of developing funnel cloud. The location of the tornado at this time is shown in Fig. 5.

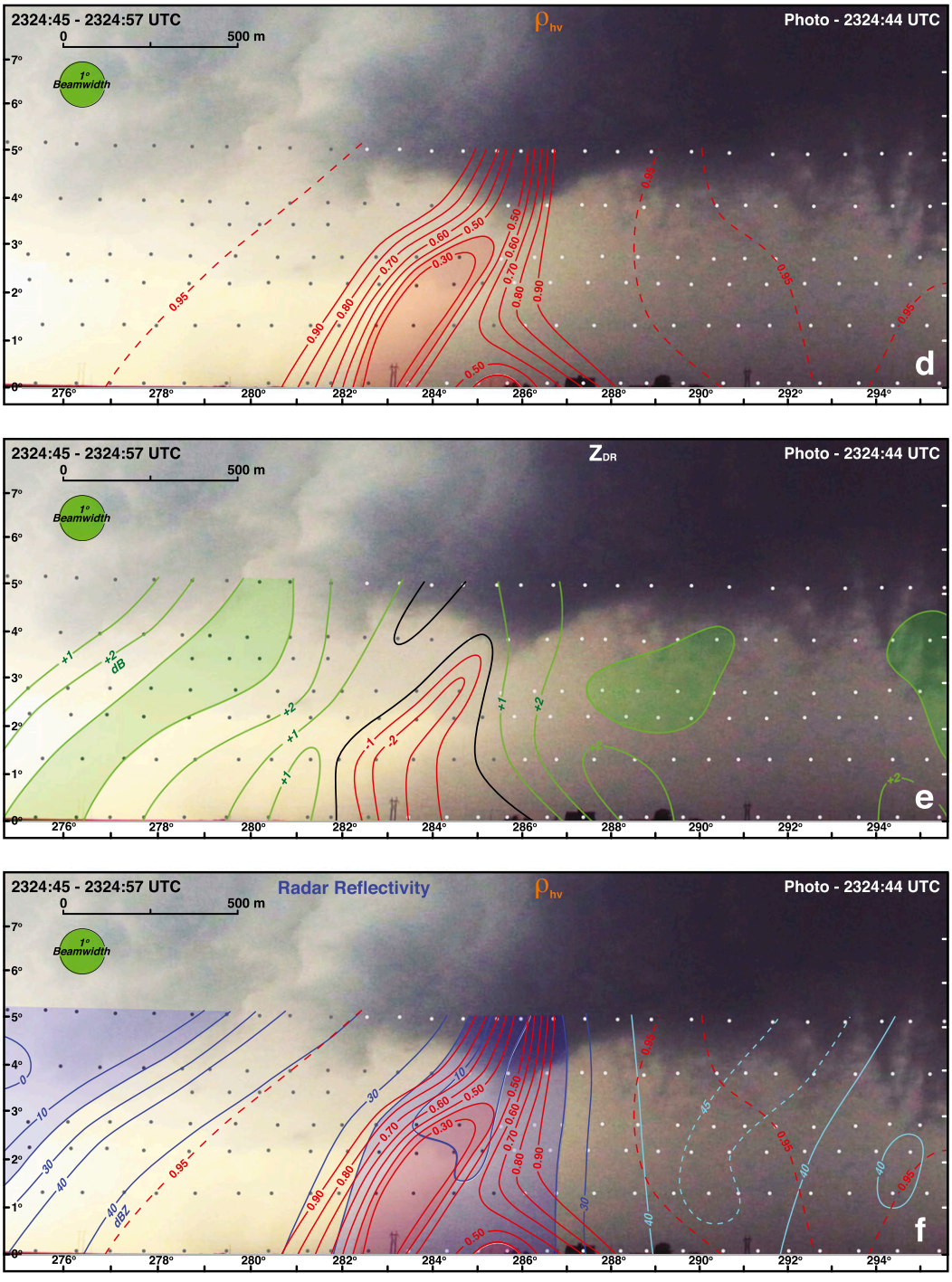

FIG. 7. (*Continued*)

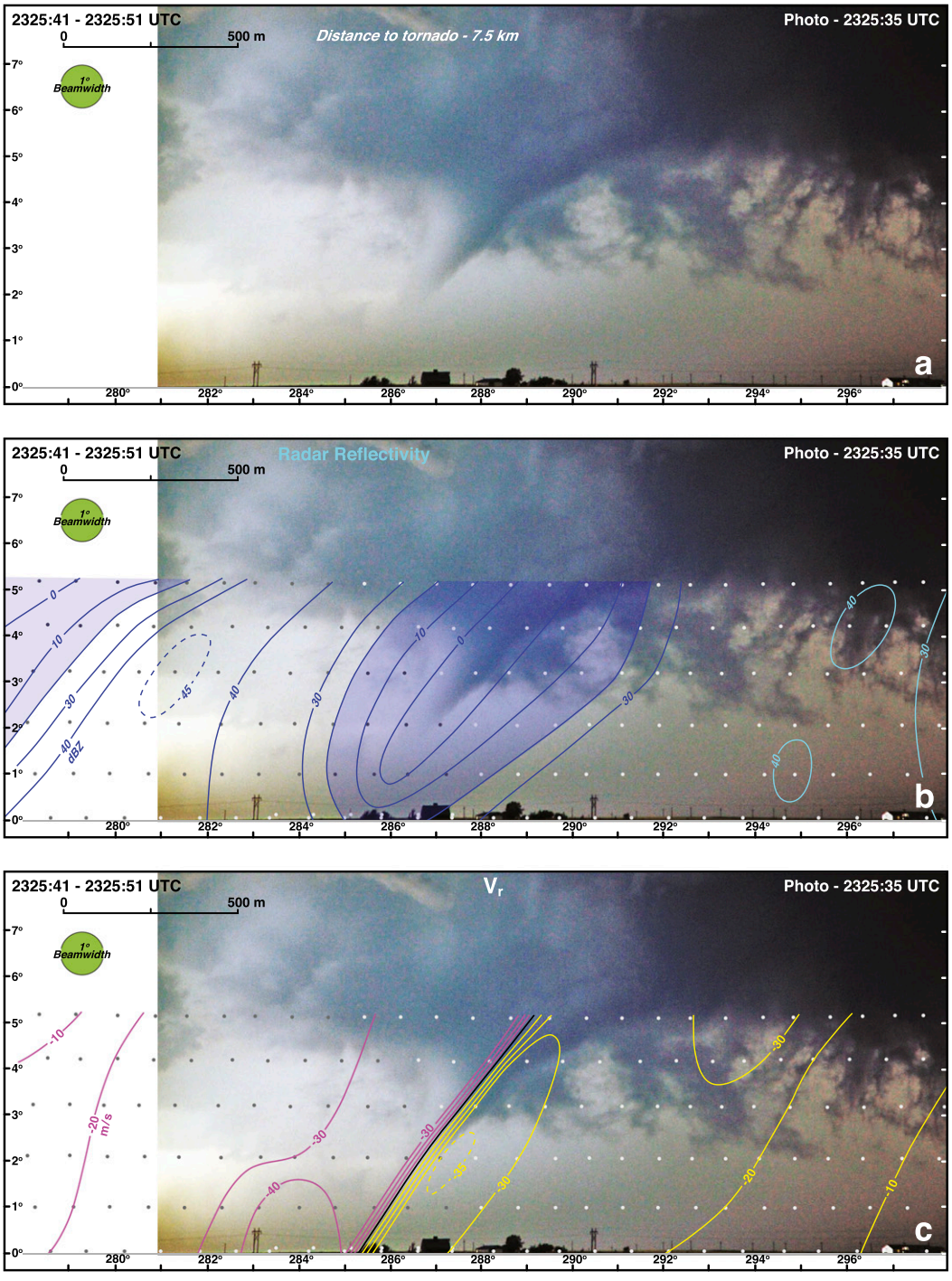

FIG. 8. (a) Photograph of Dodge City tornado 4 at 2325:35 UTC. Radar volume scan is 2325:41–2325:51 UTC. (b) Radar reflectivity (dBZ). Values < 20 dBZ are shaded light blue. (c) Ground-relative single-Doppler velocities ($m\,s^{-1}$). Magenta and yellow lines are isopleths of approaching and receding single-Doppler velocities, respectively. (d) Cross-correlation coefficient ρ_{hv}. Values < 0.40 are shaded red. (e) Differential reflectivity Z_{DR}. Red and green lines are isopleths of negative and positive Z_{DR}, respectively; $Z_{DR} > 3$ dB are shaded green. (f) Radar reflectivity and ρ_{hv}. The green circle represents the 1° beamwidth of the radar. The scales labeled in the figures are valid at the distance to the center of the tornado. The small dots represent the raw data points from RaXPol. The location of the tornado at this time is shown in Fig. 5.

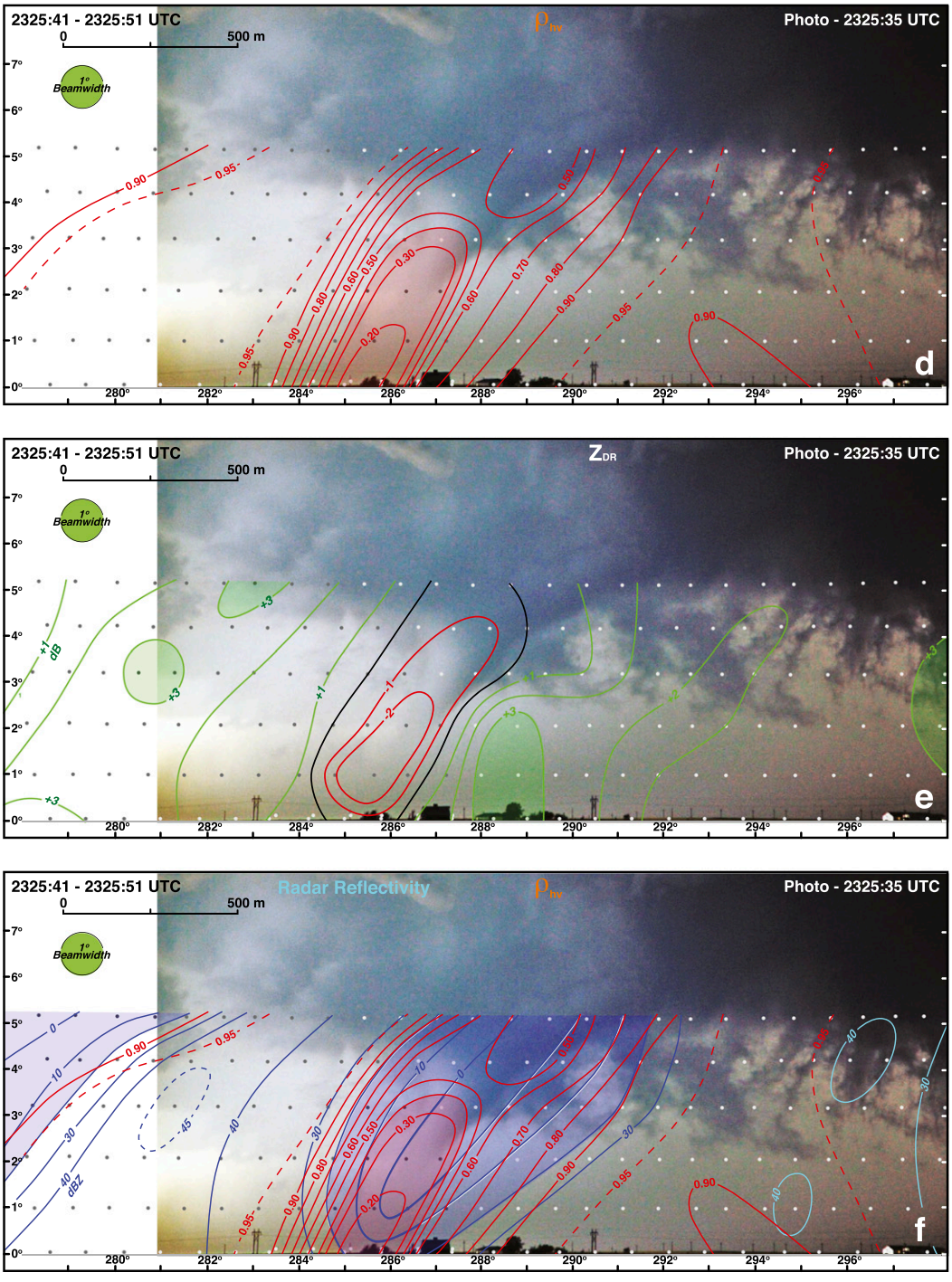

FIG. 8. (*Continued*)

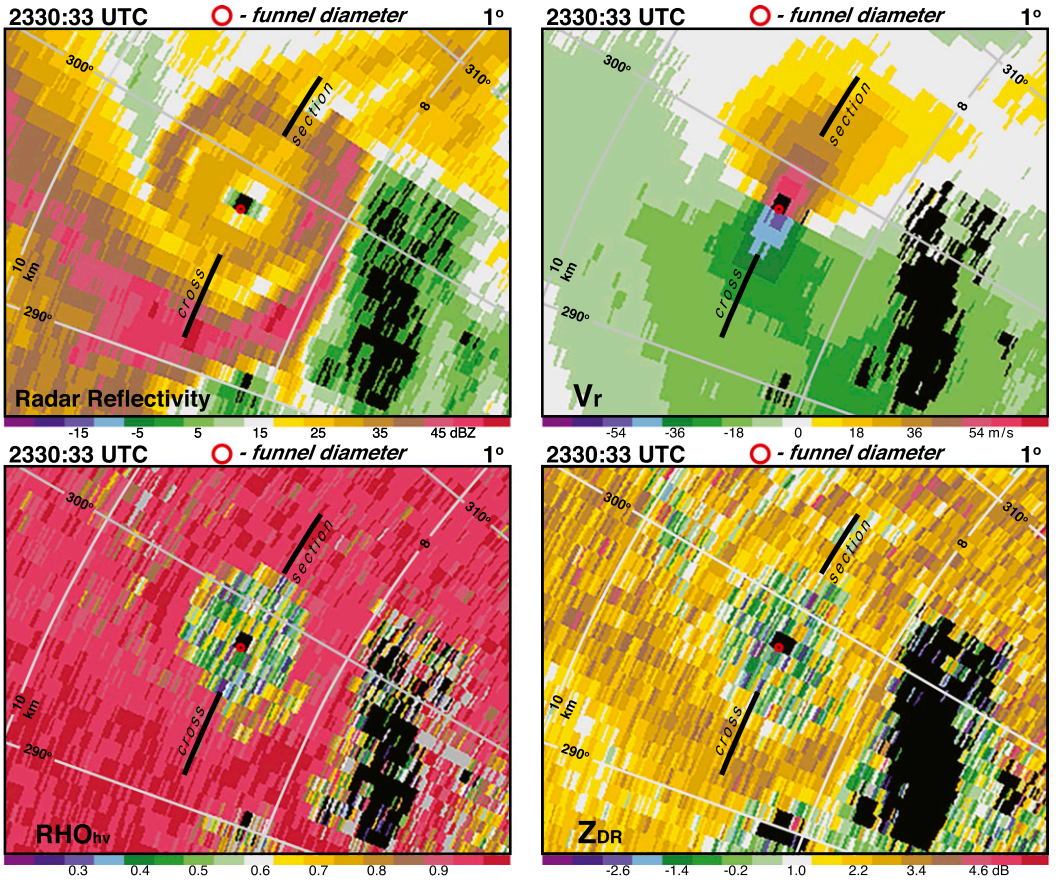

FIG. 9. Radar reflectivity, single-Doppler velocities V_r, cross-correlation coefficient ρ_{hv}, and differential radar reflectivity Z_{DR} scans from RaXPol at 1° elevation angle at 2330:33 UTC. Range and azimuth angle grid is shown by the gray lines. Black line represents the location of the cross section shown in Fig. 10. The red circle represents the size of the funnel cloud near the surface in Fig. 10a.

tornado; however, no polarimetric data were available in their study. The widths of the WEC and debris field defined by lower ρ_{hv} are comparable (Fig. 8f) in contrast to the results shown by Wakimoto et al. (2015) and Houser et al. (2016). This difference is not surprising since the tornadoes in their studies were more intense and were associated with large amounts of lofted debris. The negative column of Z_{DR} extending into cloud base within the WEC remains a prominent feature (Fig. 8e). Areas of positive Z_{DR} (>3 dB) indicative of large raindrops encompass the tornado (Fig. 8e). The trough of ρ_{hv} and the WEC both centered on the funnel cloud leads to the conclusion that this region is composed of a low concentration of very small debris even in the presence of strong centrifuging. Low Z_{DR} (Fig. 8e) also suggests an absence of hydrometeors. These observations are consistent with simulations by Lewellen et al. (2008) depicting a central tornado core that is sporadically populated by sand even in the presence of centrifuging.

c. 2330:32–2330:46 UTC

The funnel cloud depicted in Fig. 8a dissipates at ~2326 UTC even though a tornado is still apparent owing to a well-defined damage track and rotational couplet (not shown). Another funnel cloud forms at ~2327 UTC, briefly reaches the surface, before transitioning into a funnel aloft at ~2327:45 UTC. The funnel cloud remains aloft and does not reach surface again until ~2330 UTC and remains in contact with the surface during the observational period. A TDS was continuously identified in the RaXPol scans from 2326–2330 UTC; however, no lofted debris could be visually identified in any of the photographs or videos (not shown). A small WEH has developed within the hook echo at 2330:33 UTC and is accompanied by a strong rotational couplet (Fig. 9). The widths of the regions of low ρ_{hv} and Z_{DR} have also increased (Fig. 9). The red circle in Fig. 9 denotes the width of the funnel cloud near the surface and is plotted on subsequent figures of low-level scans recorded by RaXPol. The circle provides an important perspective

on the size of the tornado in relation to the much larger radar signatures shown in these figures.

The funnel cloud accompanying tornado 4 at 2330:33 UTC is shown in Fig. 10a. The WEC has narrowed near the surface from the previous analysis time and the minimum radar reflectivities are now less than −5 dBZ in response to the intensifying circulation with large regions where the velocities exceed 50 m s^{-1} (Fig. 10c). The motion of the tornado away from RaXPol (Fig. 5) is contributing to the observed asymmetry in radial velocities depicted in Fig. 10c. The annulus of high radar reflectivities surrounding the WEC can be identified near the surface (between 290°–293° and 302°–303° in Fig. 10b). A new feature, however, has developed just outside of the WEC. A smaller annulus of strong echoes has developed within a few hundred meters of the visible funnel cloud (highlighted by the black arrows in Fig. 10b). The inner and outer tubes or rings of high reflectivity can also be identified in the RaXPol scan shown in Fig. 9. The reflectivity pattern shown Figs. 9 and 10b is the double-ring structure noted by past investigators (e.g., Wurman et al. 1996; Wurman and Gill 2000; Tanamachi et al. 2007; Kosiba et al. 2008; Wakimoto et al. 2011). They proposed that the inner ring was associated with lofted debris while the outer ring was associated with precipitation. Bluestein et al. (2007b) concluded that the inner ring of a hook echo was the result of lofted debris using dual-polarization measurements at X band. The Z_{DR} and ρ_{hv} scans shown in Fig. 9 are consistent with these past studies.

The vertical profile in ρ_{hv} (Fig. 10d and 10f) reveals a different pattern than the previous times. A trough of ρ_{hv} is still centered on the funnel cloud. However, prominent in the lower half of the vertical cross section of ρ_{hv} are two areas of low ρ_{hv} surrounding the funnel cloud (black arrows in Fig. 10d). These two areas are close to the inner ring of high radar reflectivity noted earlier (Fig. 10f). Low ρ_{hv} and larger values of echo intensity suggest that these are two regions of high debris loading or areas of larger debris sizes that could be present in low concentrations just outside of the funnel cloud. Similar structures have been noted by Dowell et al. (2005), Lewellen et al. (2008), and Bodine et al. (2016a) using simulations of lofted debris (Fig. 2 in Bodine et al. 2016a; Fig. 5 in Lewellen et al. 2008). The maxima in high debris loading are located near the strongest azimuthal velocities in these simulations, similar to the analyses presented in Figs. 10c and 10d. The vertical profile of Z_{DR} at low levels reveals a ring of relatively low Z_{DR} that encompasses the funnel cloud. The Z_{DR} minima are also close to the areas of low ρ_{hv}, which could indicate that the areas of relatively high debris loading may be characterized by some common alignment at this time. *This appears to be the first time that high debris loading at low levels seen in simulations has been verified in observations*. The column of high Z_{DR} located south of the funnel cloud is still apparent.

d. 2331:27–2331:42 UTC

The funnel cloud widens and a lofted debris/dust cloud can now be seen at low levels during the 2331:27–2331:42 UTC volume scan (Fig. 11a). The minimum radar reflectivities are still low (<0 dBZ) and the 20-dBZ isopleth is now located above the surface and near the top of the visible debris cloud (Fig. 11b). The increase in echo intensity near the ground is owing to an increase in lofted debris as the tornado intensifies and moves over a dirt field (Fig. 5). The speeds within the rotational couplet continue to increase with the maximum azimuthal velocities located near the edge of the funnel cloud (Fig. 11c). The column of minimum ρ_{hv} is more pronounced in response to the increase in lofted debris and still extends throughout the funnel cloud and WEC (Figs. 11d and 11f). The black arrows in Figs. 11b and 11d denote low-level regions of high radar reflectivity and low ρ_{hv}, respectively, which were noted in Fig. 10 where high debris/particle loading is occurring. Pockets of positive Z_{DR} (highlighted by the black arrows) are also apparent at this time in contrast to the earlier analysis. The large Z_{DR} encompassing the funnel cloud at low levels was only observed during this analysis time and may be a result of hydrometeors that were entrained into the lofted debris. It is possible that hydrometeors could have fallen from above after exiting the updraft. Common debris alignment (horizontally oriented particles) is also a plausible explanation.

The low ρ_{hv} region has begun to extend farther to the south of the tornado (293°–297° in Fig. 11d) when compared to the profile shown in Fig. 10d. Examination of the RaXPol scans revealed that the low ρ_{hv} is a result of strong wind speeds in the inflow that are progressively lofting small debris and dust as air moves into and rotates around the weak echo notch of the hook echo (also shown in Fig. 12) as proposed by Ryzhkov et al. (2005) and Wakimoto et al. (2016). Indeed, note that the extension of the area of low ρ_{hv} is located in the weak echo region of the hook in Fig. 11f. The funnel cloud is embedded in a region of negative Z_{DR} but there is also another column of negative Z_{DR} (<−3 dB) located on the southern periphery of the funnel, which may indicate common debris alignment in this region resulting from the strong inflow drawing debris into the region.

e. 2332:04–2332:18 and 2333:00–2333:14 UTC

The low-levels scans of radar reflectivity and single-Doppler velocities recorded by RaXPol at 2332:05 UTC

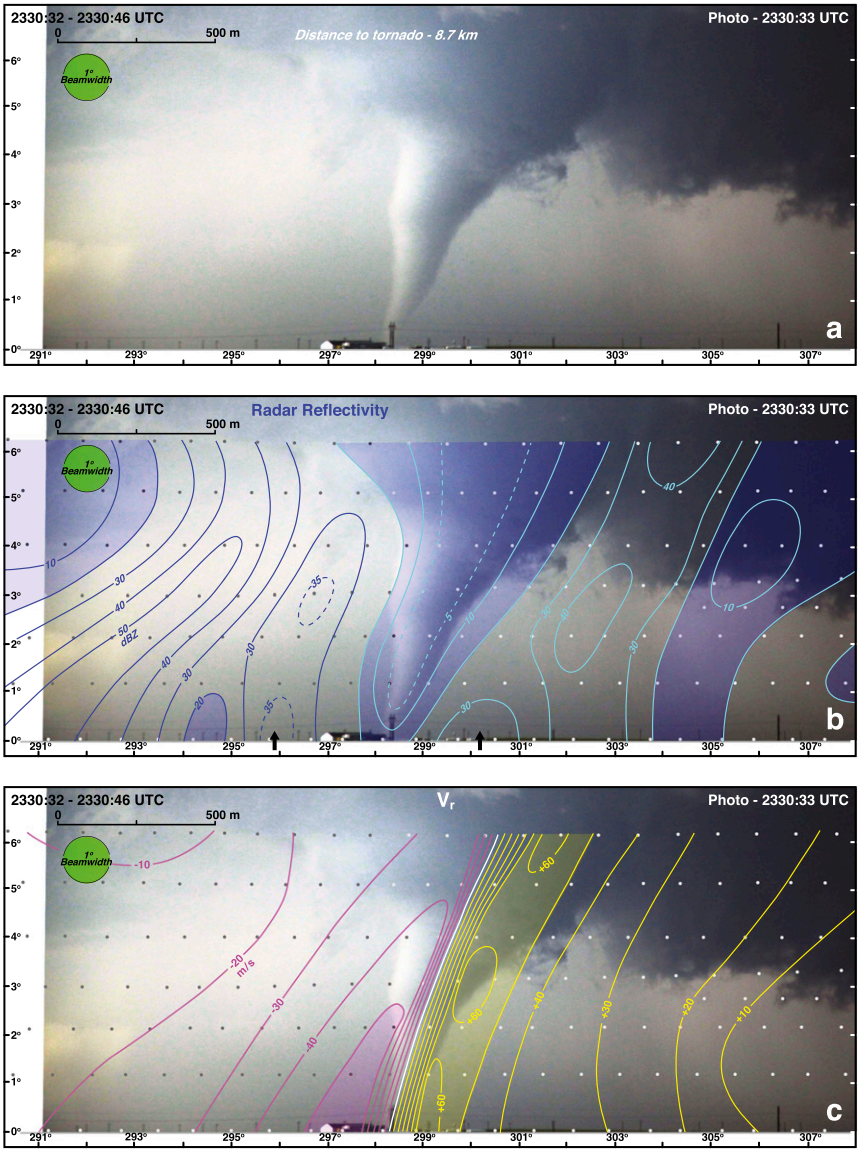

FIG. 10. (a) Photograph of Dodge City tornado 4 at 2330:33 UTC. Radar volume scan is 2330:32–2330:46 UTC. (b) Radar reflectivity (dBZ). Values < 20 dBZ are shaded light blue. (c) Ground-relative single-Doppler velocities (m s^{-1}). Magenta and yellow lines are isopleths of approaching and receding single-Doppler velocities, respectively. Velocities <-50 and >50 m s^{-1} are shaded light magenta and yellow, respectively. (d) Cross-correlation coefficient ρ_{hv}. Values < 0.40 are shaded red. (e) Differential reflectivity Z_{DR}. Red and green lines are isopleths of negative and positive Z_{DR}, respectively; $Z_{DR} > 3$ dB are shaded green. (f) Radar reflectivity and ρ_{hv}. The green circle represents the 1° beamwidth of the radar. The scales labeled in the figures are valid at the distance to the center of the tornado. The black arrows in (b) and (d) denote regions of higher radar reflectivity and low ρ_{hv}, respectively. The small dots represent the raw data points from RaXPol. The location of the tornado at this time is shown in Fig. 5.

(Fig. 12) have not changed drastically compared to Fig. 9 although the azimuthal shear is stronger. A semicircular ring of low ρ_{hv} (black arrow) outlining small lofted debris rotating around the WEH mentioned earlier surrounds the TDS signature. A circular band of positive Z_{DR} is denoted by the black arrow and is a result of hydrometeors within the band of high radar reflectivity that has coiled up around the WEH.

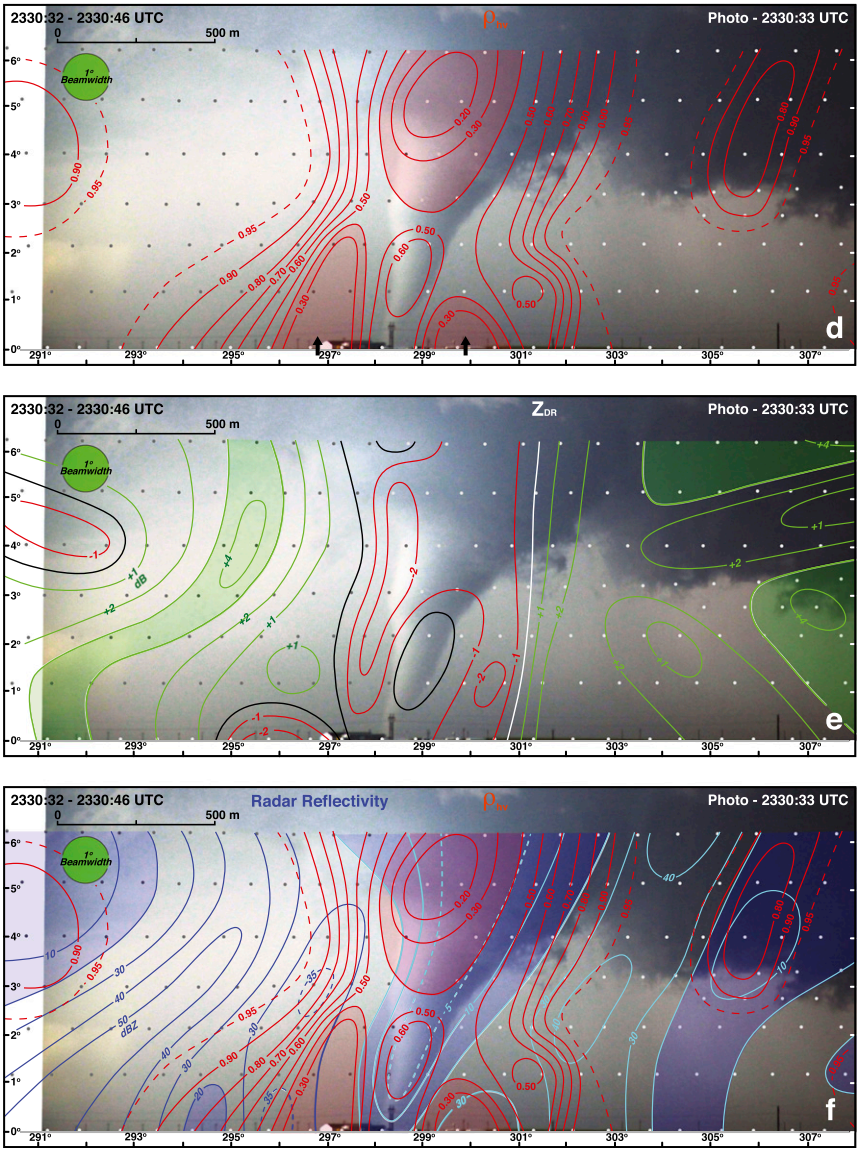

FIG. 10. (*Continued*)

The funnel cloud continues to widen and the debris cloud is more distinctive near the surface and now covers ~1/3 of the visible funnel cloud (Fig. 13a). The WEC is still well defined and the inner ring of the high radar reflectivity at low levels (denoted by the black arrows) is still apparent (Fig. 13b). The low-level rotational couplet (denoted by the black arrows) continues to intensify and is associated with differential radial velocities >151 m s^{-1} (Fig. 13c). The column of low ρ_{hv} is collocated with the funnel cloud with pockets of low ρ_{hv} flanking the funnel at low levels (denoted by the black arrows) near the inner ring of high radar reflectivity. The observations shown in Figs. 13d and 13f appear to be characteristic features of the ρ_{hv} signature of lofted debris for this particular tornado. The vertical structure of the small lofted debris particles (low ρ_{hv}) advecting into the weak echo notch of the hook echo, highlighted in Fig. 12, south of the tornado (denoted by the black arrow at ~295° in Figs. 13d and 13f) is clearly apparent.

Figures 14 and 15 were created in order to facilitate comparisons between the photogrammetric analyses of the radar reflectivity and ρ_{hv} fields, respectively, with the data recorded at 1° elevation angle by RaXPol. The relationship of the vertical profile of radar reflectivity with the RaXPol scan (Fig. 14) is aided by the rotation of the latter so that the radar azimuth angle to the tornado is aligned with the photographer's view of the tornado

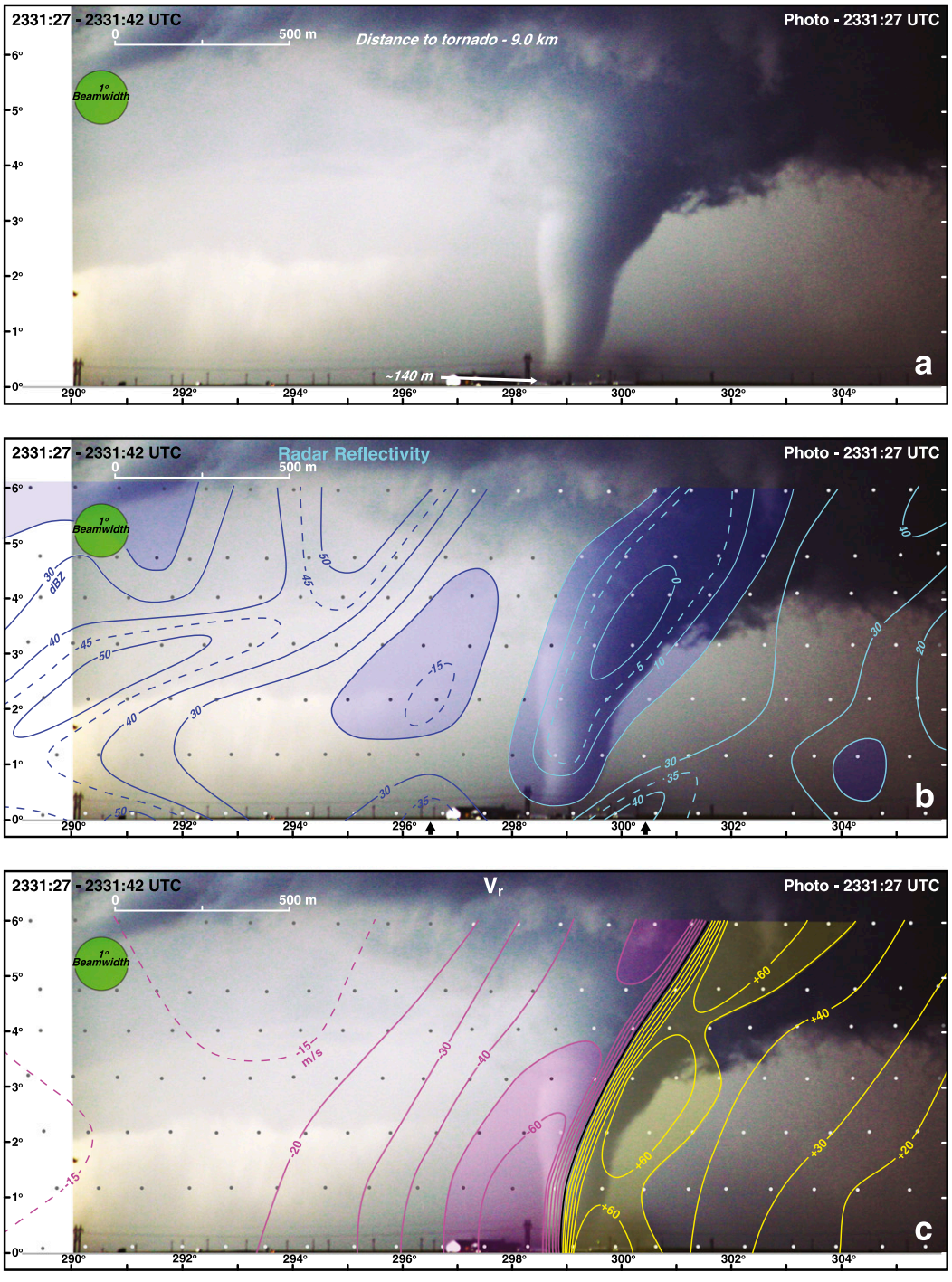

FIG. 11. (a) Photograph of Dodge City tornado 4 at 2331:27 UTC. Radar volume scan is 2331:27–2331:42 UTC. (b) Radar reflectivity (dBZ). Values < 20 dBZ are shaded light blue. (c) Ground-relative single-Doppler velocities (m s^{-1}). Magenta and yellow lines are isopleths of approaching and receding single-Doppler velocities, respectively. Velocities < -50 and > 50 m s^{-1} are shaded light magenta and yellow, respectively. (d) Cross-correlation coefficient ρ_{hv}. Values < 0.40 are shaded red. (e) Differential reflectivity Z_{DR}. Red and green lines are isopleths of negative and positive Z_{DR}, respectively; $Z_{DR} > 3$ dB and < -3 dB are shaded green and red, respectively. (f) Radar reflectivity and ρ_{hv}. Black arrows in (b), (d), and (e) denote areas of high radar reflectivity, low ρ_{hv}, and high Z_{DR}, respectively. The green circle represents the 1° beamwidth of the radar. The scales labeled in the figures are valid at the distance to the center of the tornado. The small dots represent the raw data points from RaXPol. The location of the tornado at this time is shown in Fig. 5.

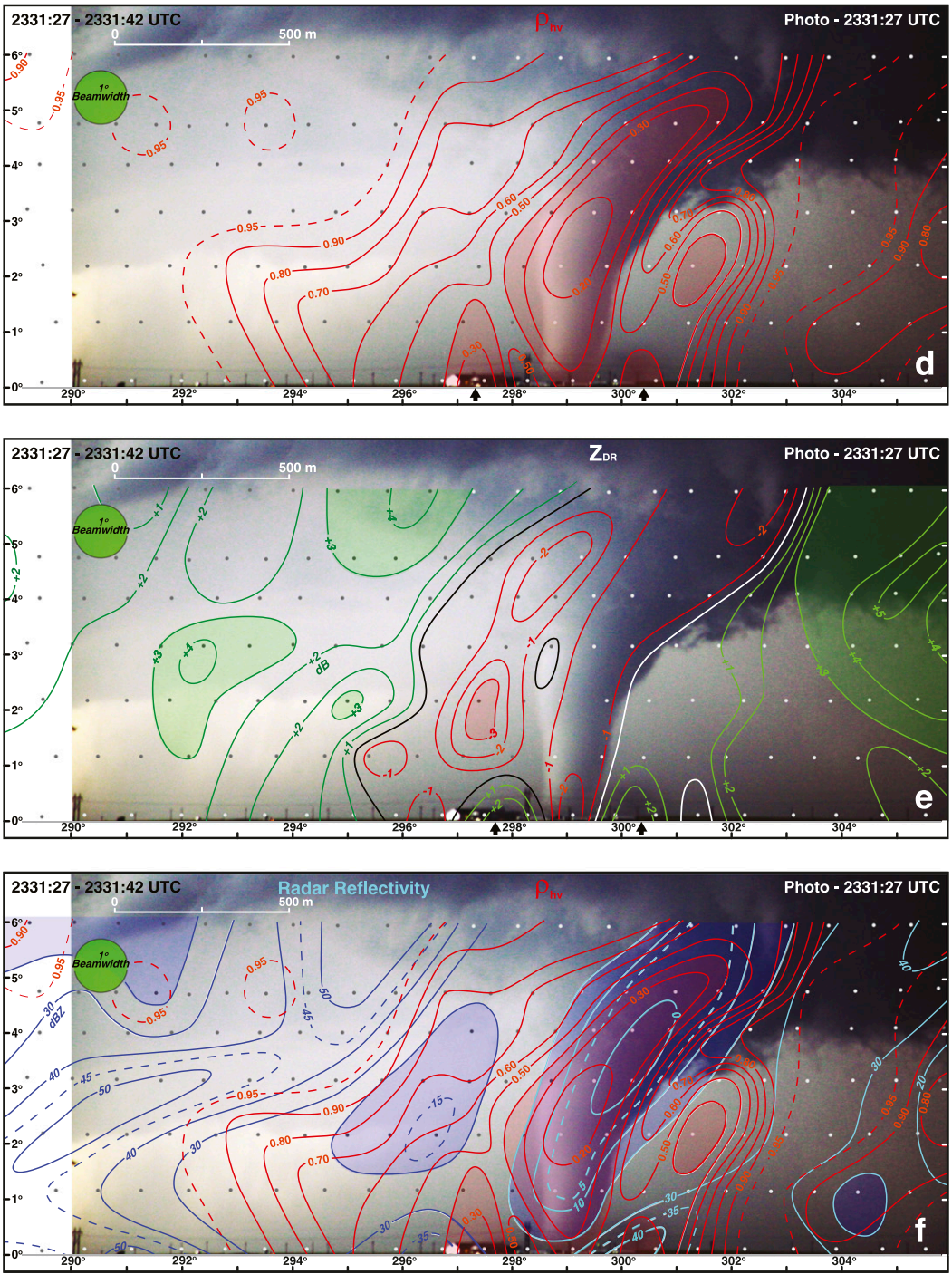

FIG. 11. (*Continued*)

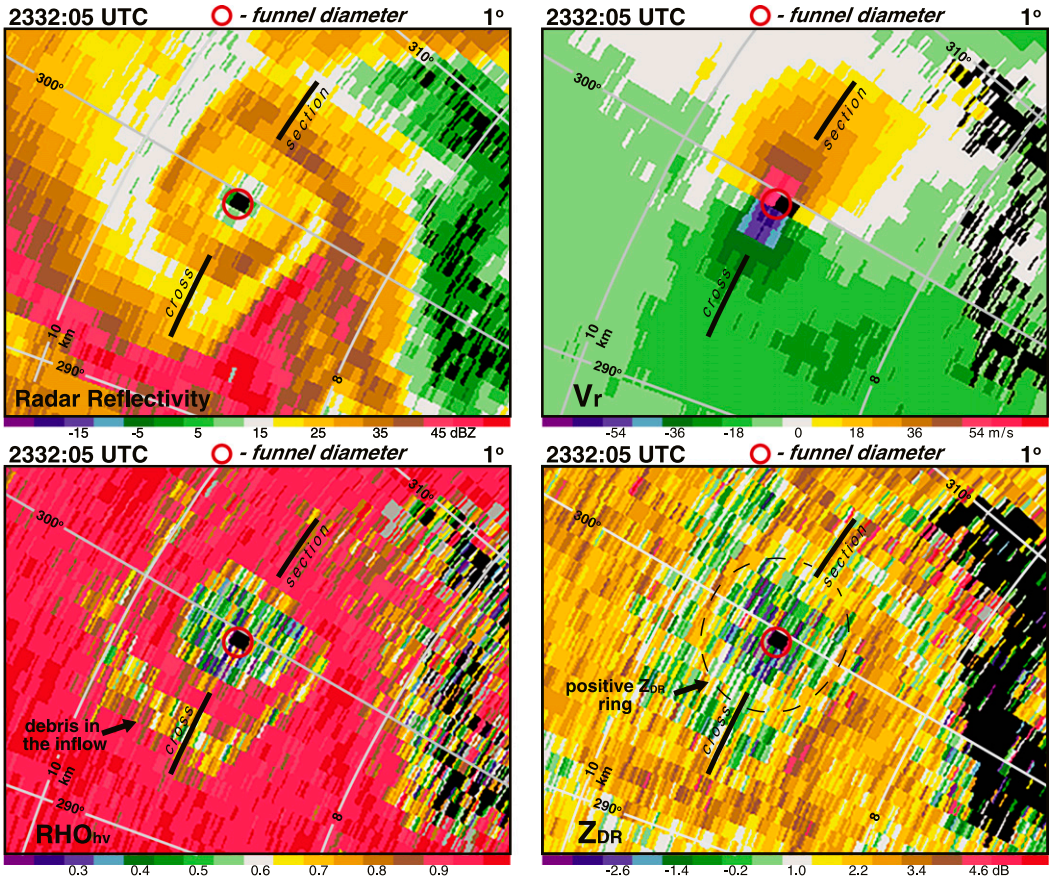

FIG. 12. Radar reflectivity, single-Doppler velocities V_r, cross-correlation coefficient ρ_{hv}, and differential radar reflectivity Z_{DR} scans from RaXPol at 1° elevation angle at 2332:05 UTC. Range and azimuth angle grid is shown by the gray lines. Black line represents the location of the cross section shown in Fig. 13. The red circle represents the size of the funnel cloud near the surface in Fig. 13a. Black arrow on the ρ_{hv} plot denotes a region where small debris has been lofted by inflow rotating within the weak echo notch of the hook echo. The black arrow on the Z_{DR} plot denotes a ring of relatively high Z_{DR}.

(i.e., note that the 300° azimuth angle for the top and bottom images are aligned in Fig. 14). The size of the funnel cloud in comparison to the hook echo is apparent since the length scales for both images in the figure are equal. The TDS as viewed in the 1° elevation scan can also be readily compared to the vertical profile of ρ_{hv} and the funnel cloud shown in the photogrammetric analysis (Fig. 15). The previously mentioned low ρ_{hv} signature spiraling within the weak echo notch of the hook echo at the 1° elevation angle scan is aligned with the same feature in the vertical profile in Fig. 15.

The negative Z_{DR} column is, once again, collocated with the funnel cloud surrounded by positive Z_{DR}. The low-level pockets of positive Z_{DR} near the funnel (black arrows in Fig. 13e) is the Z_{DR} ring shown in Fig. 12. Two other region of high Z_{DR} (shaded green) located at a larger radius are also noted and have been a relative consistent feature in these vertical profiles. A polarimetric signature that could be uniquely equated to the visual debris cloud is not readily identifiable. The small size of lofted dust may preclude these particles from substantially impacting the TDS at the X band since other larger scatterers may dominate the backscattered returns. In addition, the radar receives backscattered signal from particles with different dielectric constants while the visual observations are a result of scattered and reflected visible light. Accordingly, the discrepancy may not be surprising. There are no substantive changes to the kinematic structure of the WEC (Fig. 16b) but the debris cloud continues to widen at 2333:00–2333:14 UTC (Fig. 16a). The analysis of low ρ_{hv} at the location of the tornado is now characterized with multiple minima in the column (Fig. 16c) compared to the earlier time (Fig. 13d). The major difference in the ρ_{hv} field is the lofted debris signature contained with the weak echo notch, which now has

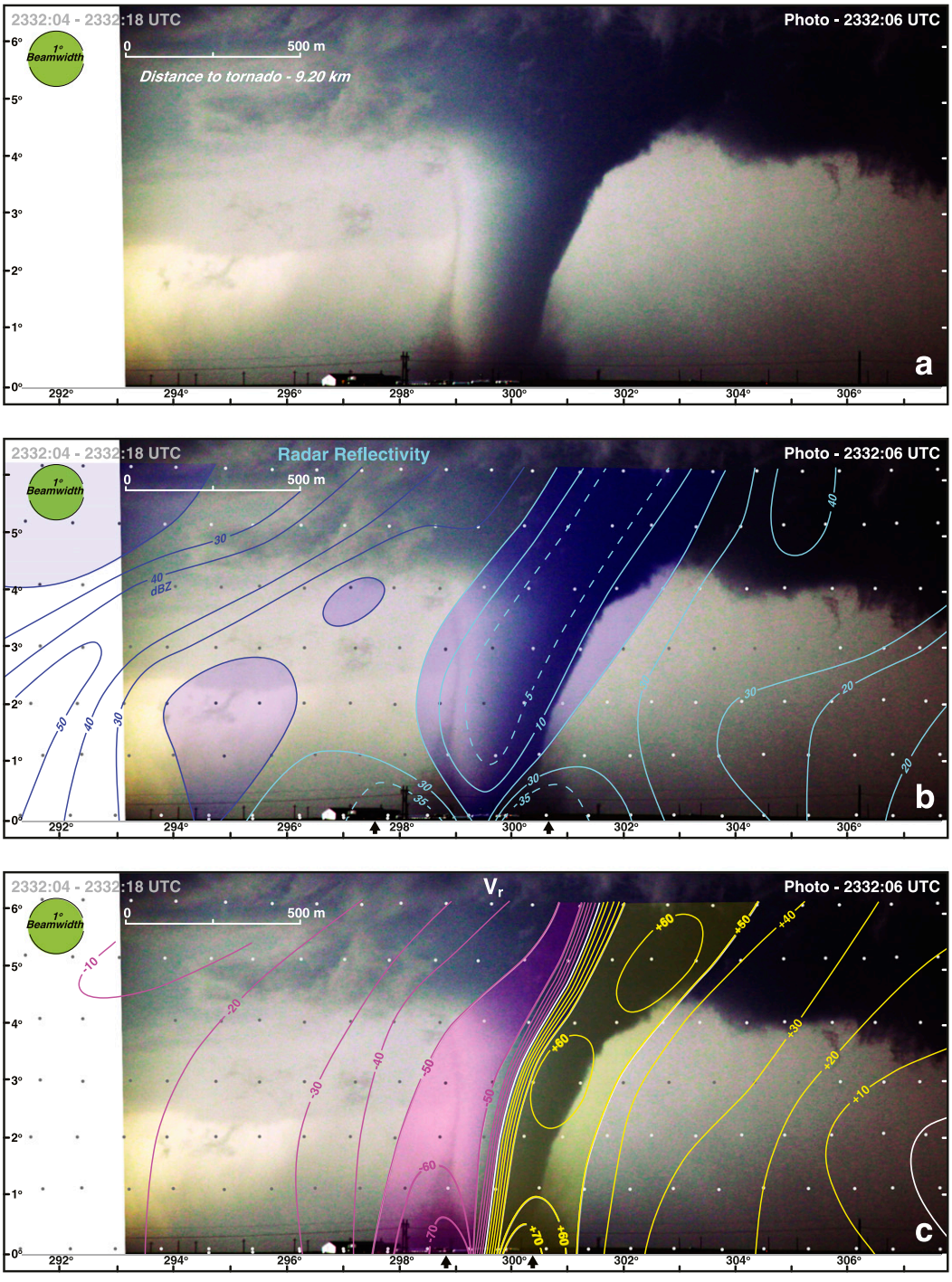

FIG. 13. (a) Photograph of Dodge City tornado 4 at 2332:06 UTC. Radar volume scan is 2332:04–2332:18 UTC. (b) Radar reflectivity (dBZ). Values < 20 dBZ are shaded light blue. (c) Ground-relative single-Doppler velocities ($m\,s^{-1}$). Magenta and yellow lines are isopleths of approaching and receding single-Doppler velocities, respectively. Velocities < -50 and $> 50\ m\,s^{-1}$ are shaded light magenta and yellow, respectively. (d) Cross-correlation coefficient ρ_{hv}. Values < 0.40 are shaded red. (e) Differential reflectivity Z_{DR}. Red and green lines are isopleths of negative and positive Z_{DR}, respectively; $Z_{DR} > 3$ dB and < -3 dB are shaded green and red, respectively. (f) Radar reflectivity and ρ_{hv}. Black arrows in (b), (c), and (e) denote areas of high radar reflectivity, low-level rotational couplet, and high Z_{DR}, respectively. Black arrows in (d) denote low ρ_{hv} near the funnel and another area of low ρ_{hv} in the inflow region. The green circle represents the 1° beamwidth of the radar. The scales labeled in the figures are valid at the distance to the center of the tornado. The small dots represent the raw data points from RaXPol. The location of the tornado at this time is shown in Fig. 5.

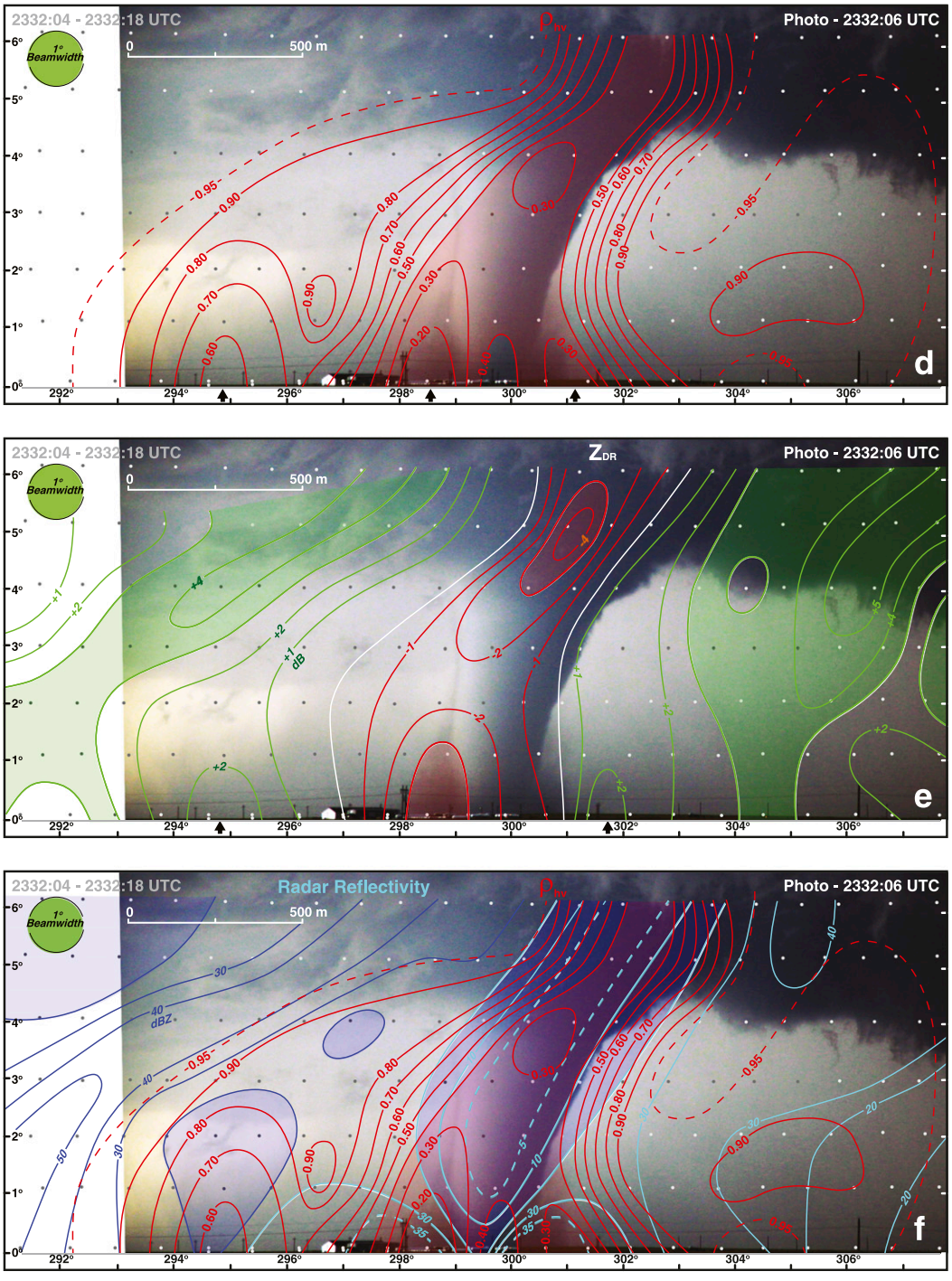

FIG. 13. (*Continued*)

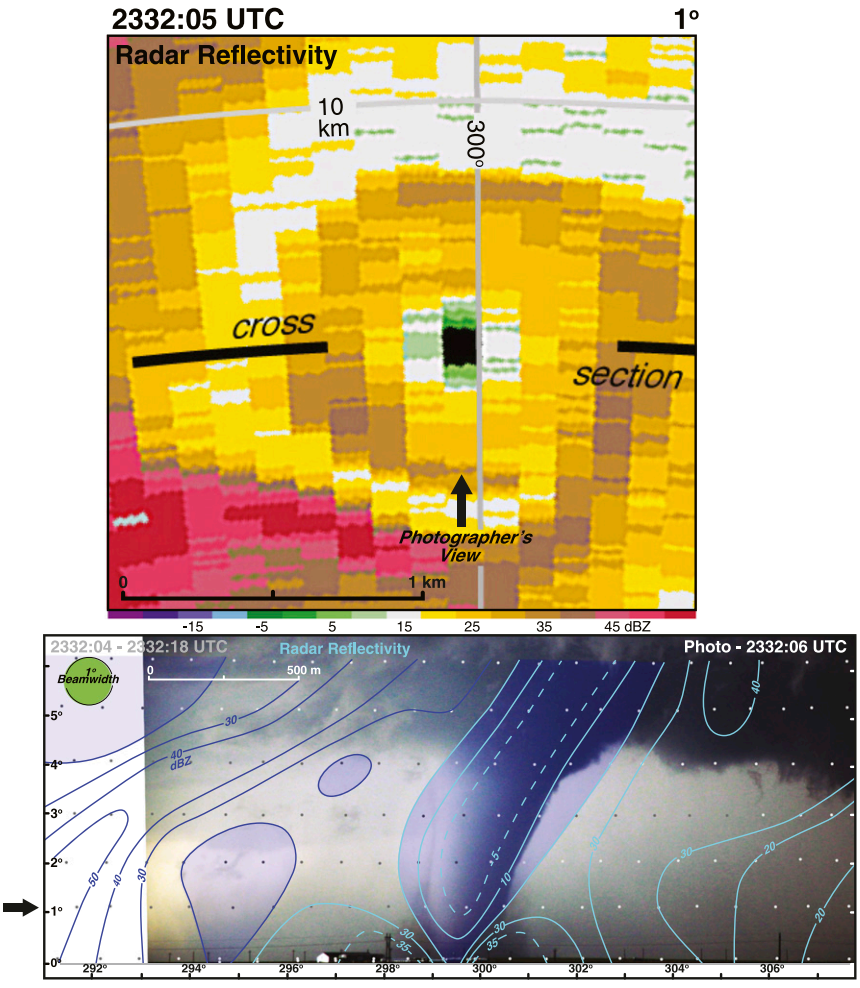

FIG. 14. (top) Radar reflectivity scan from RaXPol at 1° elevation angle at 2332:05 UTC. Range and azimuth angle grid is shown by the gray lines. Viewing angle of the photograph taken of the tornado is shown by the black arrow. Black line represents the location of the cross section shown below. (bottom) The analysis as is shown in Fig. 13b. Black arrow denotes the location of the 1° elevation angle scan. The length scale for the radar reflectivity scan and photogrammetric analysis at the distance of the tornado are the same.

been lofted to a height of ~800 m, near the base, and has resulted in another column of relatively low ρ_{hv}.

f. 2333:54–2334:08 UTC

The funnel cloud begins to narrow near the ground; however, the rotational couplet continues to intensify during the next two volume scans (not shown). The debris cloud surrounding the funnel cloud can be clearly identified during the 2333:54–2334:08 UTC volume scan (Fig. 17a). Similar debris clouds have been documented in photographs (e.g., Bluestein et al. 2007b, see their Fig. 12) and in numerical simulations (e.g., Lewellen et al. 2008, see their Fig. 1). The portion of the lofted debris that is nearly opaque reaches a height of ~250 m but the translucent part of the debris cloud extends to near the cloud base in the figure. The increase in the amount of visible debris lofted is in response to the increasing wind speeds and not related to the tornado passing over a surface that is characterized by debris that could be easily lofted even if the tornado wind speeds remained constant. Indeed, an aerial photograph of the field that the tornado traversed during four times analyzed in this paper is shown in Fig. 18 (magenta circles). The dirt field had been recently plowed. The tornado was north of the driveway at the time of the analysis shown in Fig. 17. The yellow line in Fig. 18 encompasses an area ~400 m in width where dirt has been scoured. The scouring is consistent with the visual growth of the debris cloud at 2333:52 UTC.

There is an increase in debris loading both visually and in the documented increase in radar reflectivity at his

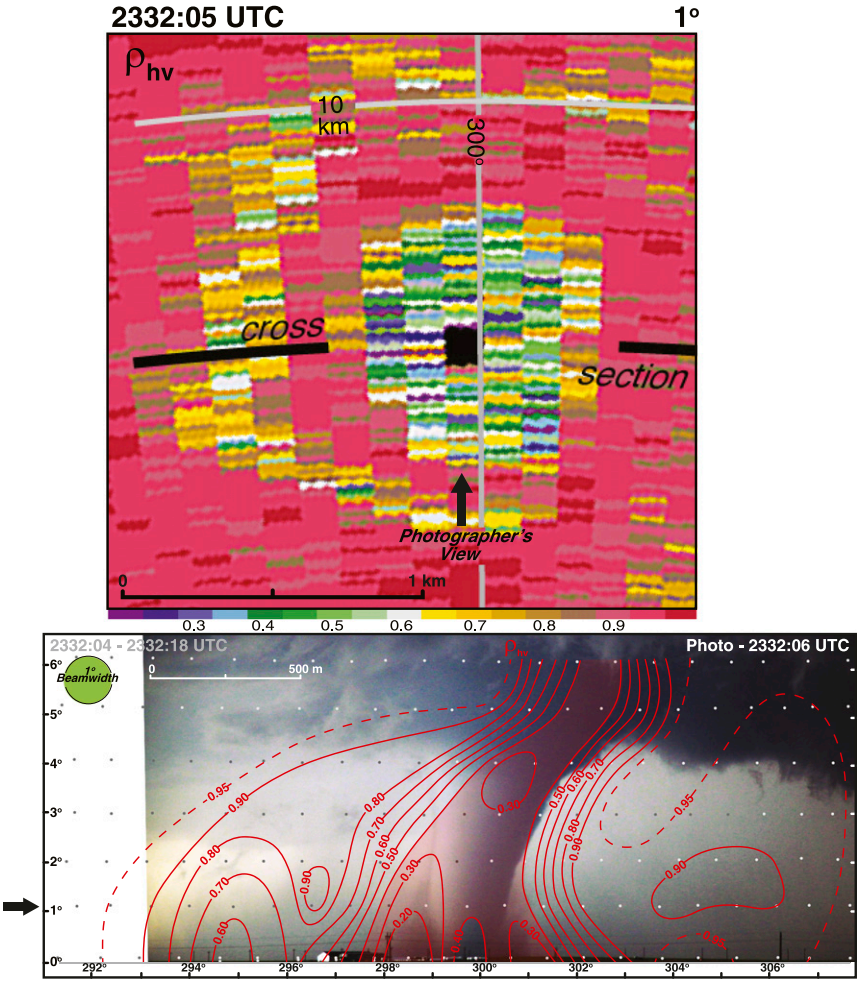

FIG. 15. (top) Cross-correlation coefficient scan from RaXPol at 1° elevation angle at 2332:05 UTC. Range and azimuth angle grid is shown by the gray lines. Viewing angle of the photograph taken of the tornado is shown by the black arrow. Black line represents the location of the cross section shown below. (bottom) The same analysis shown in Fig. 13d. Black arrow denotes the location of the 1° elevation angle scan. The length scale for the radar reflectivity scan and photogrammetric analysis at the distance of the tornado are the same.

time. However, this increase in debris loading does not appear to result in a decrease in the tornado's wind speeds (as measured by the Doppler velocities) as shown in debris simulations. It is possible that either the amount of lofted debris was insufficient to impact the tornadic wind speeds or that the storm/tornado-scale processes that increased the tornado's intensity had a greater influence than any changes caused by debris loading.

The WEC has narrowed in width and is elevated above the surface (Fig. 17b). The tube of high radar reflectivity (highlighted by the black arrows) has increased and is now >50 dBZ suggesting relatively high concentration of debris are being lofted into these regions. The 40-dBZ isopleth approximately outlines the main portion of the debris cloud that overlaps with the most intense region of the rotational couplet (Fig. 17c). The black arrow in Fig. 17a denotes a notch in the debris cloud and a hint of a curl that has been noted before in the literature (e.g., Dowell et al. 2005, see their Fig. 12). Debris is initially lofted in a thin layer and advected inward by convergence into the tornado at low levels. The debris rises upward and is subsequently centrifuged outward. As the debris exits the updraft, the debris cloud has been observed to curl downward.

The ρ_{hv} field undergoes a dramatic evolution at this time (Figs. 17d and 17f). The column of minimum ρ_{hv} has shifted away from the tornado and WEC and is now positioned along the periphery of the funnel. The black arrows denote the two pockets of low ρ_{hv} (Fig. 17d) that has been a consistent feature during the entire

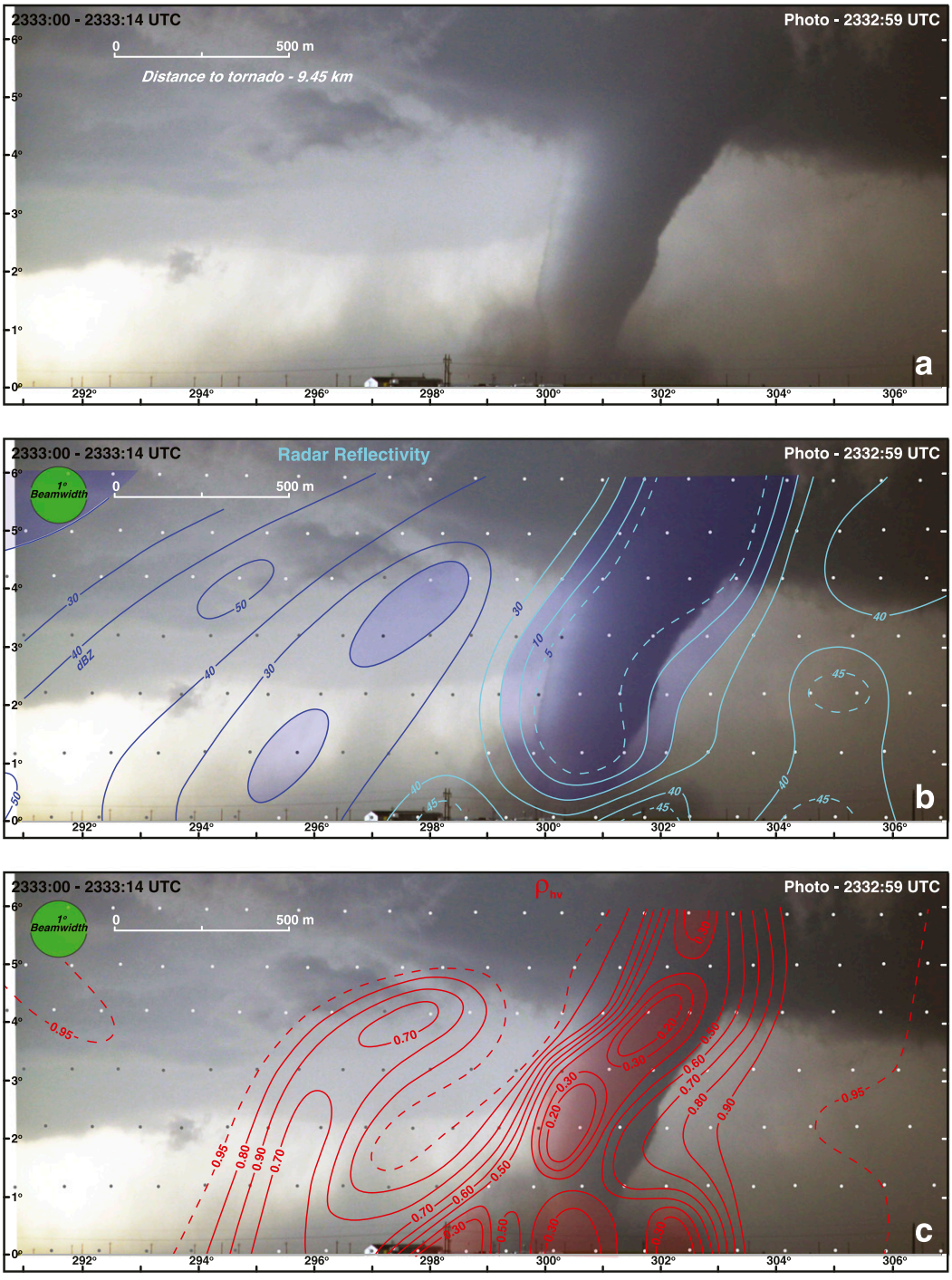

FIG. 16. (a) Photograph of Dodge City tornado 4 at 2332:59 UTC. Radar volume scan is 2333:00–2333:14 UTC. (b) Radar reflectivity (dBZ). Values < 20 dBZ are shaded light blue. (c) Cross-correlation coefficient ρ_{hv}. Values < 0.40 are shaded red. The green circle represents the 1° beamwidth of the radar. The scales labeled in the figures are valid at the distance to the center of the tornado. The small dots represent the raw data points from RaXPol. The location of the tornado at this time is shown in Fig. 5.

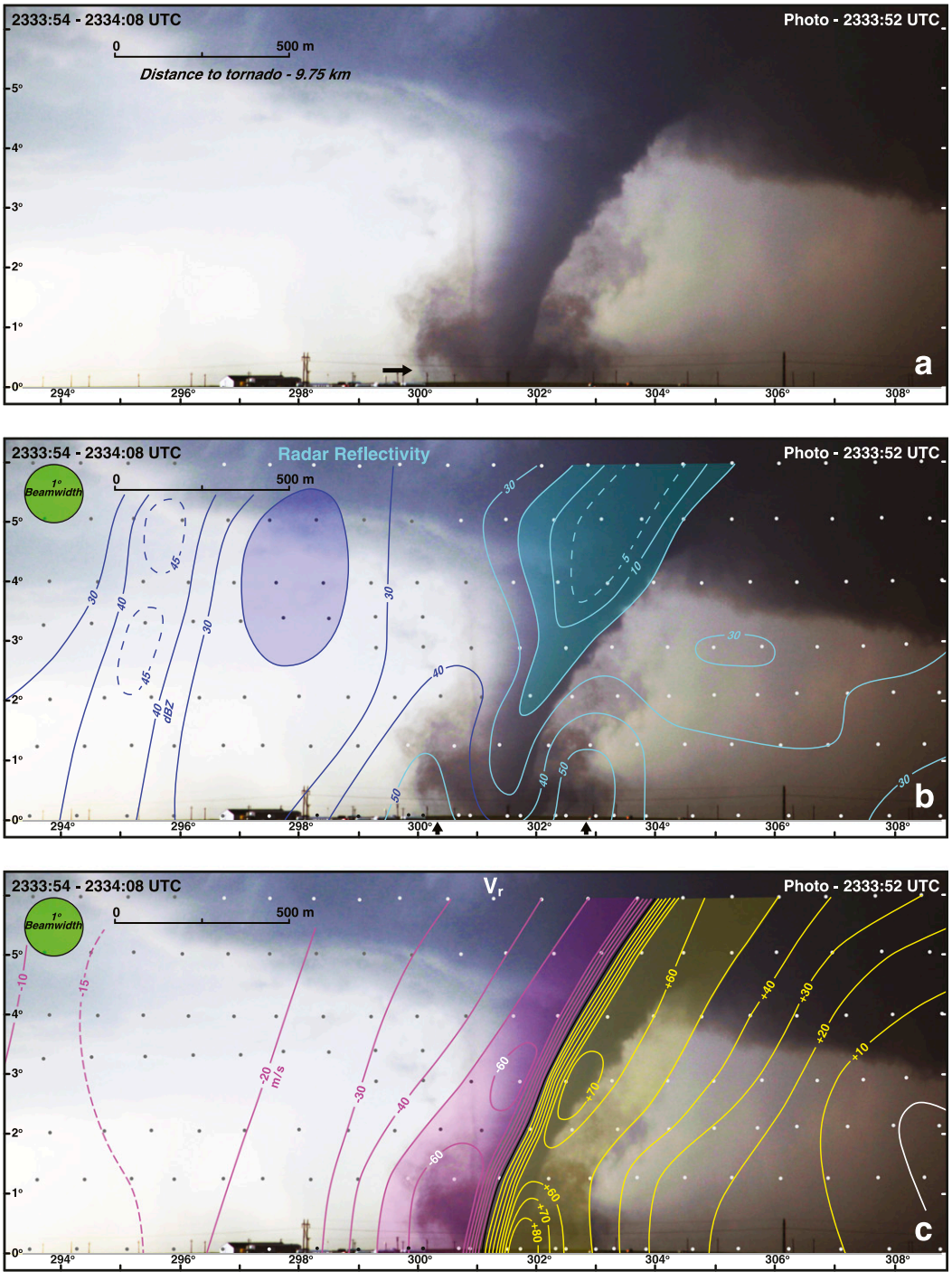

FIG. 17. (a) Photograph of Dodge City tornado 4 at 2333:52 UTC. Radar volume scan is 2333:54–2334:08 UTC. (b) Radar reflectivity (dBZ). Values < 20 dBZ are shaded light blue. (c) Ground-relative single-Doppler velocities ($m\,s^{-1}$). Magenta and yellow lines are isopleths of approaching and receding single-Doppler velocities, respectively. Velocities < -50 and > 50 $m\,s^{-1}$ are shaded light magenta and yellow, respectively. (d) Cross-correlation coefficient ρ_{hv}. Values < 0.40 are shaded red. (e) Differential reflectivity Z_{DR}. Red and green lines are isopleths of negative and positive Z_{DR}, respectively; $Z_{DR} > 3$ dB and < -3 dB are shaded green and red, respectively. (f) Radar reflectivity and ρ_{hv}. Black arrow in (a) denotes a clear region and a curl in the debris cloud. Black arrows in (b) and (d) denote areas of high radar reflectivity and low ρ_{hv} at low levels, respectively. The green circle represents the 1° beamwidth of the radar. The scales labeled in the figures are valid at the distance to the center of the tornado. The small dots represent the raw data points from RaXPol. The location of the tornado at this time is shown in Fig. 5.

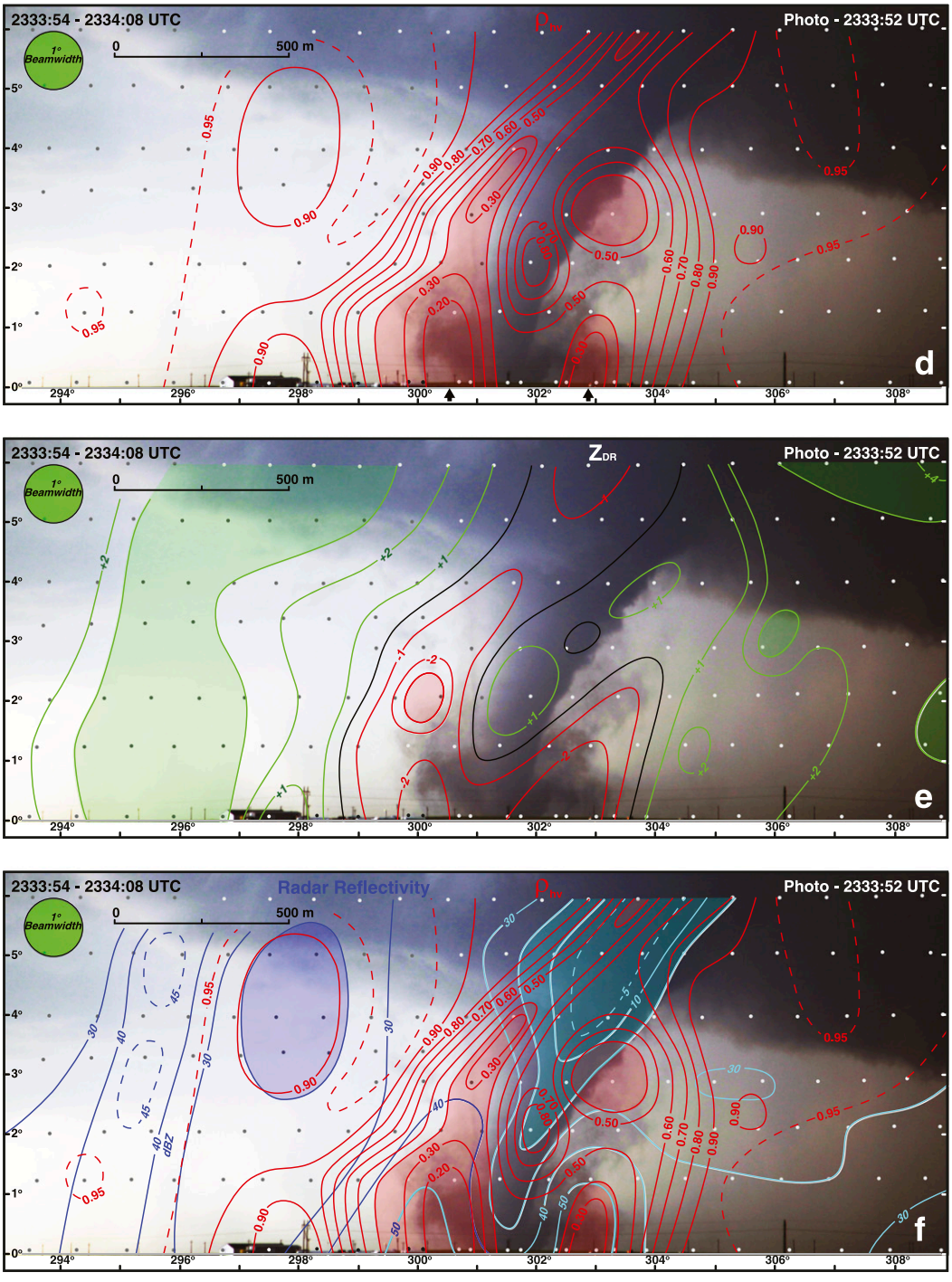

FIG. 17. (*Continued*)

FIG. 18. Aerial photo of a dirt field traversed by tornado 4. Magenta dots represent the location of tornado 4 during the analysis times shown in Figs. 13, 16, 17, and 20. Dashed line denotes the tornado path. A region of scoured dirt is enclosed by the yellow line.

observational period. These pockets are close to the visually opaque debris cloud and high radar reflectivity (Fig. 17f). The 0.90 isopleth located aloft (~500 m) at ~298° azimuth outlines the remnants of the small debris particles located in the weak echo notch of the hook echo. The Z_{DR} profile has also changed during this volume scan (Fig. 17e). Negative Z_{DR} is now located at the periphery of the funnel cloud near the areas of low ρ_{hv}. This shift in the pattern of low Z_{DR} suggests that the common debris alignment has moved from within the funnel cloud to its periphery. Negative Z_{DR} surrounding the funnel cloud was also noted in Figs. 10e and 11e. Interestingly, positive Z_{DR} is noted within the funnel cloud, which may be a result of the entrainment of hydrometeors. It is possible that vertical debris alignment of small particles still exists within the funnel cloud but the presence of a few hydrometeors has increased Z_{DR}. Horizontal debris alignment may also be occurring within the funnel cloud (e.g., Umeyama et al. 2018); however, this process alone would not fully explain the observed increases in radar reflectivity and ρ_{hv}. Low ρ_{hv} and Z_{DR} displaced from the center of the TDS has been previously noted by Griffin et al. (2017). They attribute the displacement to sub- or suction vortices revolving around the tornado center axis. This proposed mechanism does not appear to explain the polarimetric pattern shown for the Dodge City tornado. The ρ_{hv} and Z_{DR} minimum are located beyond the funnel cloud. Subvortices would not be expected to develop in this region and none were observed or resolved in the single-Doppler velocity scans.

g. 2334:29–2334:41 UTC

The TDS at 2334:31 UTC is characterized by a significant increase in radar reflectivity consistent with large amounts of lofted debris (Fig. 19). The rotational couplet has not changed appreciably when compared with the earlier scan (Fig. 12) although it is possible that the wind speeds are more intense but are difficult to resolve since the funnel is narrower than the earlier time (cf. Fig. 13a with Fig. 20a). As previously mentioned, the increase in lofted debris does not appear to be related to changes in surface characteristics (dirt field in Fig. 18). The TDS has increased in size in the ρ_{hv} and Z_{DR} fields consistent with the visual observations of the debris cloud (Fig. 20a). Low ρ_{hv} associated with small debris particles that are lofted in the inflow into the weak echo notch is less distinct compared to earlier times suggesting that these particles south of the tornado are no longer aloft. In addition, the small particles close to the tornado were likely entrained into the circulation.

The visual signature of the recirculating debris is denoted by the black arrow (Fig. 20a). The location of the curl in the visual debris has nearly doubled in height compared to the image shown in Fig. 17a. This change could be related to stronger updrafts advecting the particles to higher levels. The analysis of the RaXPol data for the 2334:29–2334:41 UTC volume scan is presented in Figs. 20b–f. The trough of radar reflectivities at the location of the tornado (Fig. 20b) is still apparent but the area <20 dBZ (shaded blue) has diminished compared to previous volume scans as a result of large amounts of debris that have been lofted. The tube of higher radar reflectivities that encompasses the funnel cloud (black arrows in Fig. 20b) extends to near the cloud base, consistent with the growth of the debris cloud. The rotational couplet at low levels (Fig. 20c) is comparable to the earlier time (Fig. 17c).

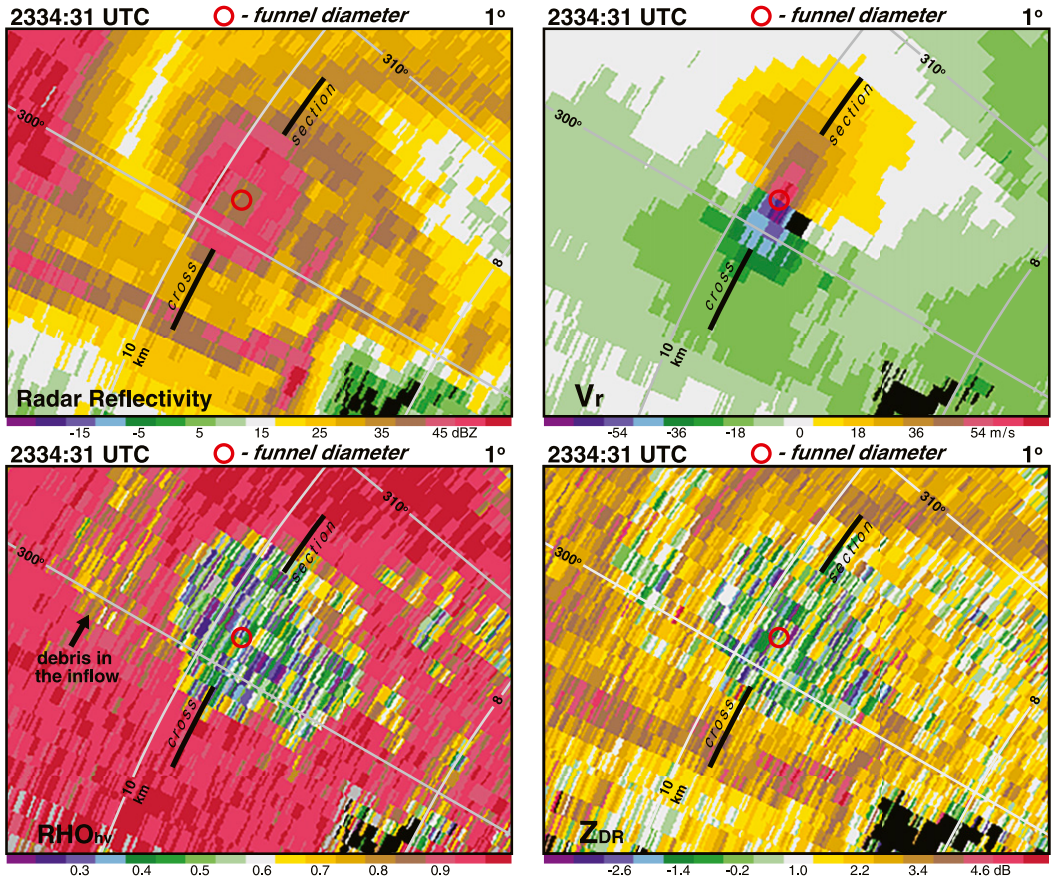

FIG. 19. Radar reflectivity, single-Doppler velocities V_r, cross-correlation coefficient ρ_{hv}, and differential radar reflectivity Z_{DR} scans from RaXPol at 1° elevation angle at 2334:31 UTC. Range and azimuth angle grid is shown by the gray lines. Black line represents the location of the cross section shown in Fig. 20. The red circle represents the size of the funnel cloud near the surface in Fig. 20a.

The cross-correlation field continues its transition from a column of minimum ρ_{hv} collocated with the funnel cloud to a ring of relatively low ρ_{hv} encircling the funnel (Figs. 20d and 20f). Low ρ_{hv} areas (shaded red) north of the funnel largely coincide with the visible debris cloud in the figure. There is less agreement between low ρ_{hv} and the debris cloud south of the funnel. Accordingly, the ρ_{hv} analysis is useful for identifying lofting of small debris particles that are not visible in photographs or movies. The Z_{DR} profile has also evolved as shown in Fig. 20e. A small region of positive Z_{DR} was apparent at the location of the tornado and was surrounded by negative Z_{DR} during the 2333:54–2334:08 UTC volume scan (Fig. 17e). A column of positive Z_{DR} (>2 dB) is now centered on the funnel cloud with regions of negative Z_{DR} encompassing the tornado approximately at the location of the debris cloud (Fig. 20e). The analysis shown in Fig. 20 suggests that larger scatterers are now present within the funnel cloud owing to the increase in radar reflectivity. In addition, these scatterers include hydrometeors (positive Z_{DR}) mixed in with lofted debris (higher ρ_{hv} in the range of 0.40–0.60). The negative Z_{DR} within the debris cloud, outside of the funnel cloud, may result from common debris alignment. As previously mentioned, debris alignment may still be occurring within the funnel cloud but that signal may be masked by the presence of hydrometeors.

4. Discussion and summary

The analysis of data recorded by RaXPol on the Dodge City, Kansas, tornado 4 represents the first attempt to combine polarimetric measurements with visual documentation of an evolving debris cloud. Previously, the relationship between the TDS and debris that was visually lofted was largely unknown. The RaXPol data also capture tornadogenesis and the formation of the funnel cloud. A detailed aerial survey determined the location of all of the tornadoes that were scanned by the radar and,

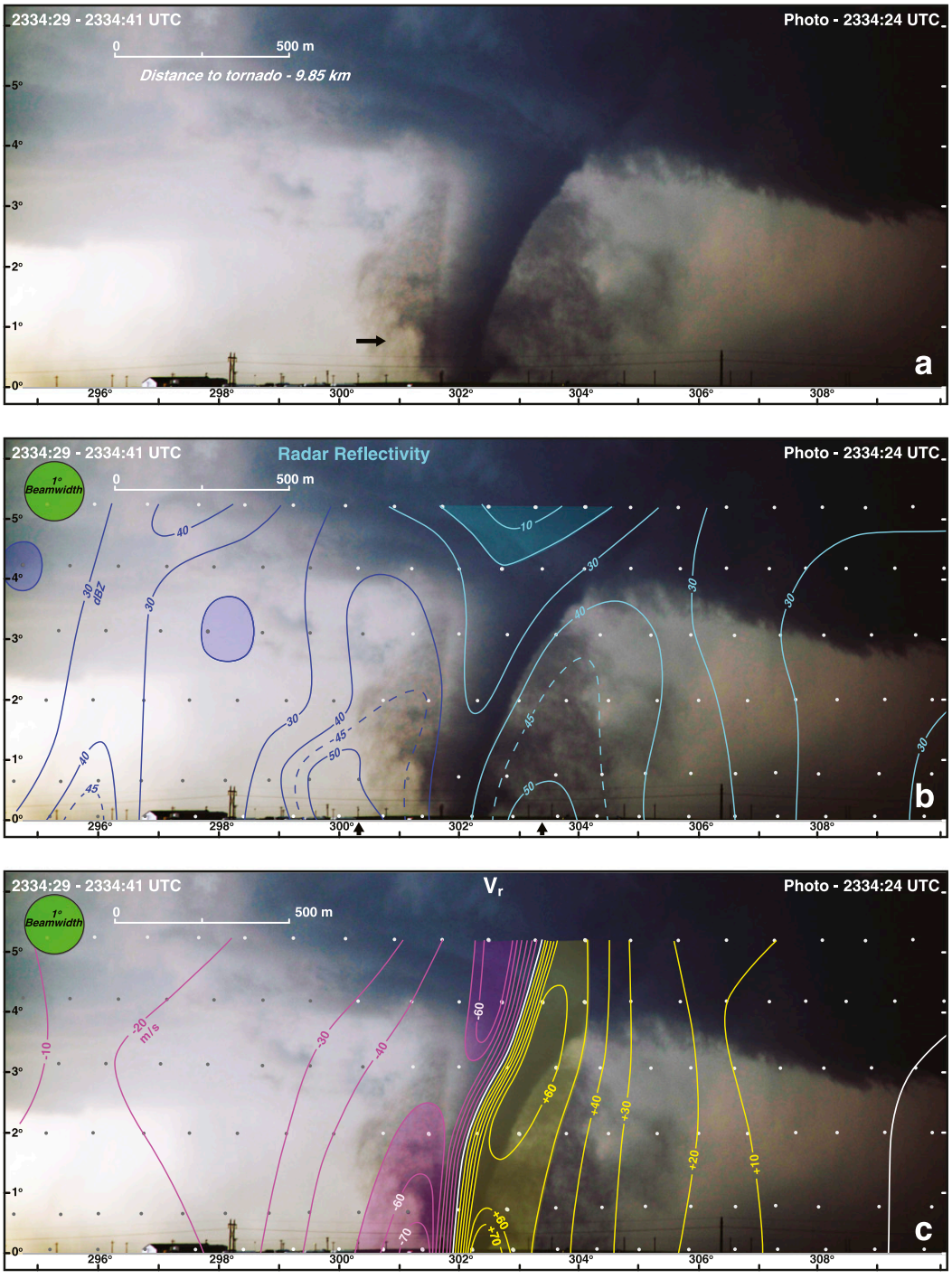

FIG. 20. (a) Photograph of Dodge City tornado 4 at 2334:24 UTC. Radar volume scan is 2334:29–2334:41 UTC. (b) Radar reflectivity (dBZ). Values < 20 dBZ are shaded light blue. (c) Ground-relative single-Doppler velocities (m s^{-1}). Magenta and yellow lines are isopleths of approaching and receding single-Doppler velocities, respectively. Velocities < -50 and > 50 m s^{-1} are shaded light magenta and yellow, respectively. (d) Cross-correlation coefficient ρ_{hv}. Values < 0.40 are shaded red. (e) Differential reflectivity Z_{DR}. Red and green lines are isopleths of negative and positive Z_{DR}, respectively; $Z_{DR} > 3$ dB and < -3 dB are shaded green and red, respectively. (f) Radar reflectivity and ρ_{hv}. Black arrow in (a) denotes a clear region and a curl in the debris cloud. Black arrows in (b) denote areas of high radar reflectivity. The green circle represents the 1° beamwidth of the radar. The scales labeled in the figures are valid at the distance to the center of the tornado. The small dots represent the raw data points from RaXPol. The location of the tornado at this time is shown in Fig. 5.

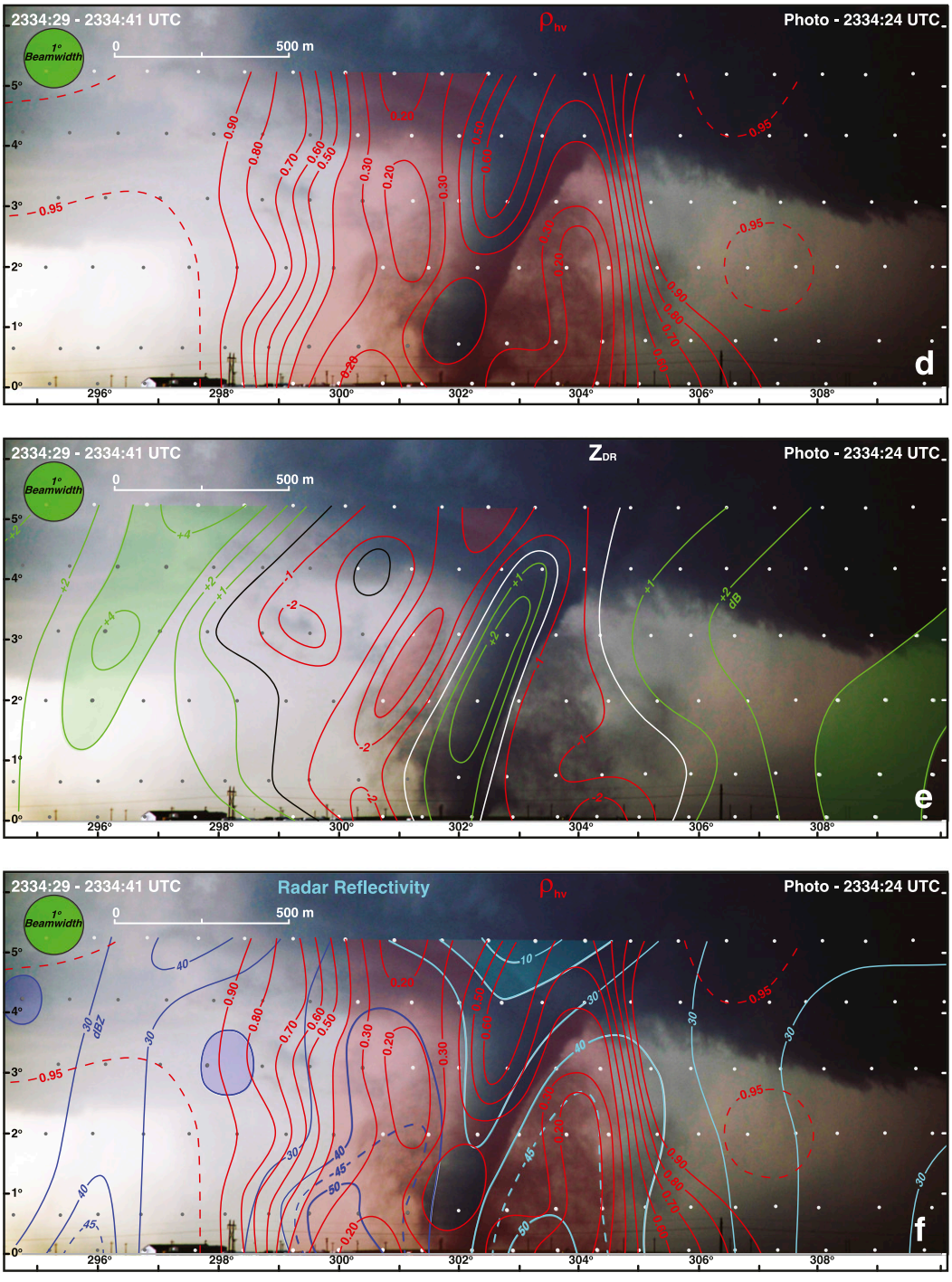

FIG. 20. (*Continued*)

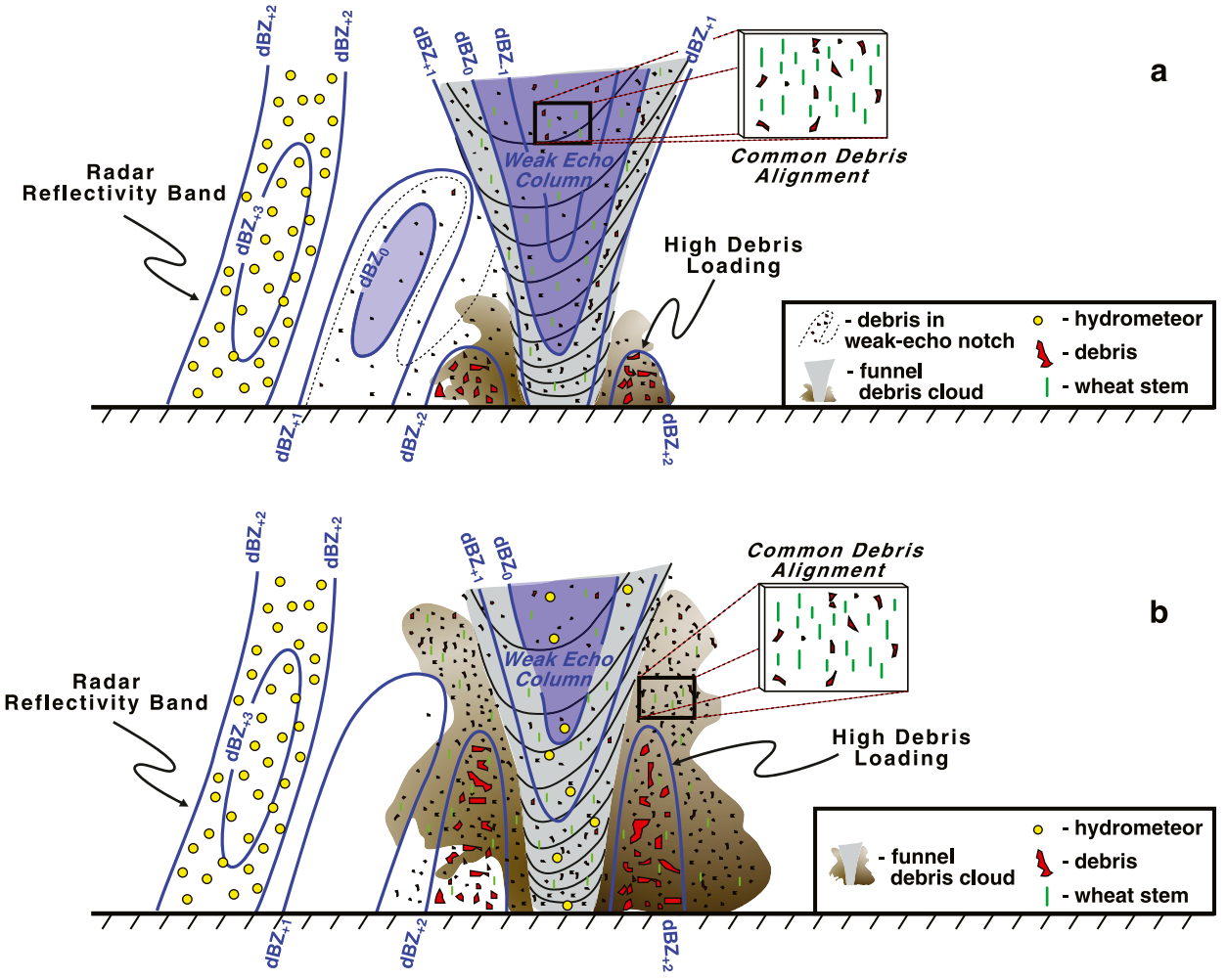

FIG. 21. Schematic models summarizing the radar reflectivity, hydrometeor, and debris fields for the Dodge City tornado for (a) early in the tornado life cycle and (b) during the time that the debris cloud encompassed the funnel cloud.

just as importantly, documented the ground cover since the characteristics of the debris cloud are strongly influenced by the surface traversed by the tornado. A WEC and the formative stage of the rotational couplet were identified during tornadogenesis. A column of low ρ_{hv} already extended to the cloud base. The existence of this column at this early stage was believed to be a combination of debris that is lofted as the wind field strengthens prior to tornadogenesis and debris fallout from the previous tornado (tornado 3) that was subsequently entrained into the tornado. A column of negative Z_{DR} was also centered on the tornado circulation and was hypothesized to result from common debris alignment (vertically oriented debris) although Mie (or resonance) scattering could also be contributing. The tornado in the present study traversed open fields that were characterized by dirt or wheat. It is unlikely that dirt would have a preferred orientation but it may be possible that wheat stems could have become vertically oriented. The wheat stems may have remained aloft even when the tornado moved over a dirt field, which would explain the persistence of the negative Z_{DR} column. Cheong et al. (2017) and Umeyama et al. (2018) used a polarimetric radar simulator to propose that common debris alignment from lofted leaves could produce a negative Z_{DR} signature. The current study has proposed that lofted wheat stems may also produce regions of common debris alignment.

An inner annulus or tube of high radar reflectivity encircled the tornado at low levels as the circulation intensified. This feature has been noted in previous studies. Two areas of low ρ_{hv} near the high echo tube were also noted and are hypothesized to be regions of high debris loading that have been documented in simulations of lofted debris. Another column of low ρ_{hv} resulted from strong wind speeds that were progressively lofting small debris and dust as inflow rotates around and within the

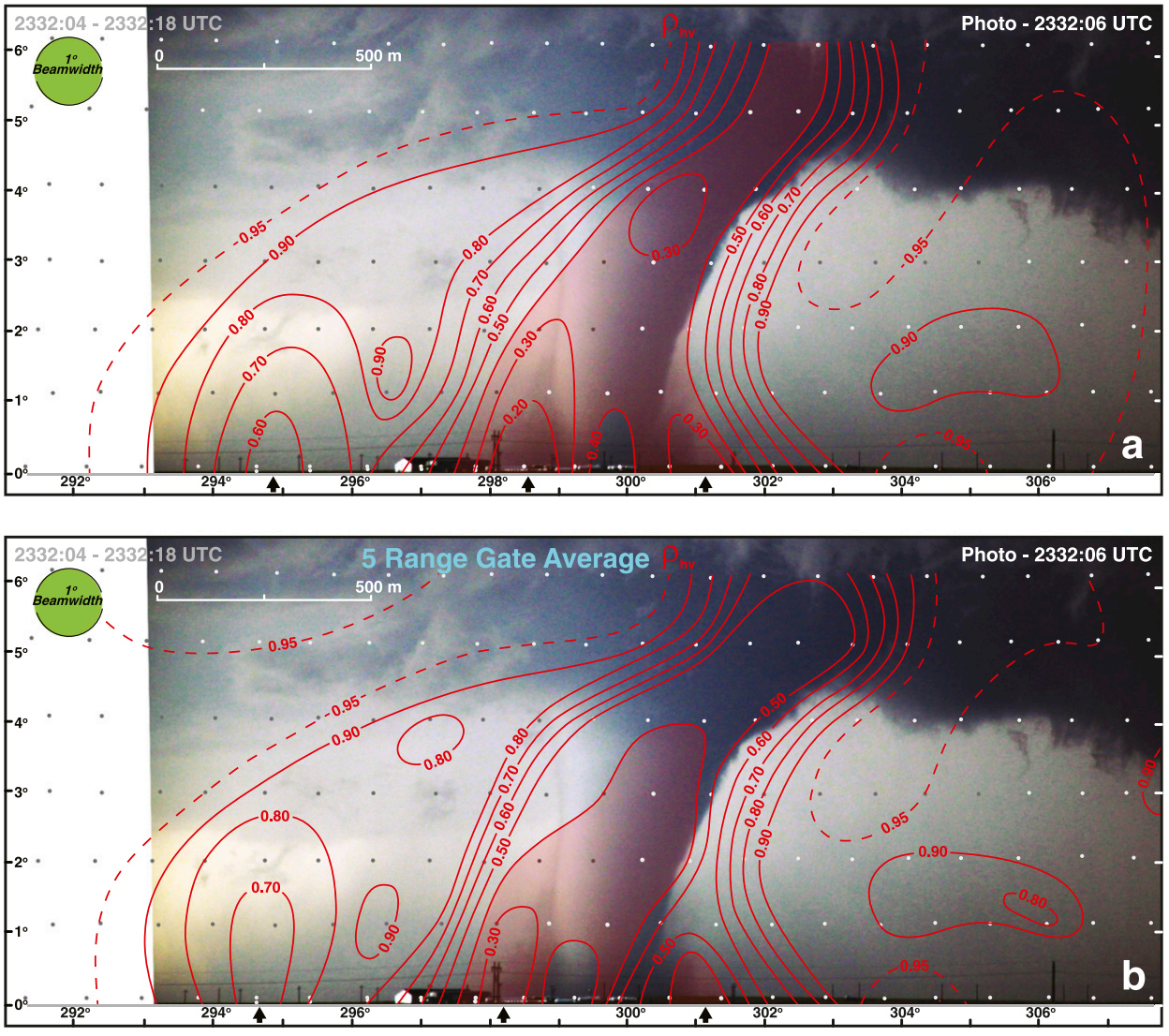

FIG. A1. Photograph of Dodge City tornado 4 at 2332:06 UTC. Radar volume scan is 2332:04–2332:18 UTC. (a) Cross-correlation coefficient (ρ_{hv}). The same cross section was presented in Fig. 13d. (b) Cross-correlation coefficient averaged over five range gates. Black arrows in (a) and (b) denote low ρ_{hv} near the funnel and another area of low ρ_{hv} in the inflow region. Values < 0.40 are shaded red. The green circle represents the 1° beamwidth of the radar. The scales labeled in the figures are valid at the distance to the center of the tornado. The small dots represent the raw data points from RaXPol.

weak echo notch of the hook echo. Debris particles in this region were lofted to near the cloud base.

The polarimetric structure undergoes a dramatic transition when the debris cloud was pronounced and enveloped most of the tornado. The WEC began to fill at lower levels as more debris was lofted into the circulation and was not centrifuged out. The minimum in ρ_{hv} was no longer located at the TDS center. Instead, it was positioned at a radius beyond the funnel cloud and approximately encompassed the visible debris cloud. A column of positive Z_{DR} was collocated with the funnel cloud and was surrounded by negative Z_{DR} that approximately encompassed the debris cloud. The positive Z_{DR} and the increase in ρ_{hv} and radar reflectivity indicate that hydrometeors may have been entrained into the tornado. The minimum in Z_{DR} and low ρ_{hv} surrounding the funnel was likely a result of common debris alignment within the debris cloud. It is also possible that vertical debris alignment was present within the funnel cloud but the polarimetric signature was masked by the hydrometeors. This hypothesis may partially explain why the Z_{DR} profiles continually evolved with time. Occasional entrainment of hydrometeors into the tornado could have shifted the axis of minimum Z_{DR} to the periphery of the funnel cloud until the hydrometeors were centrifuged.

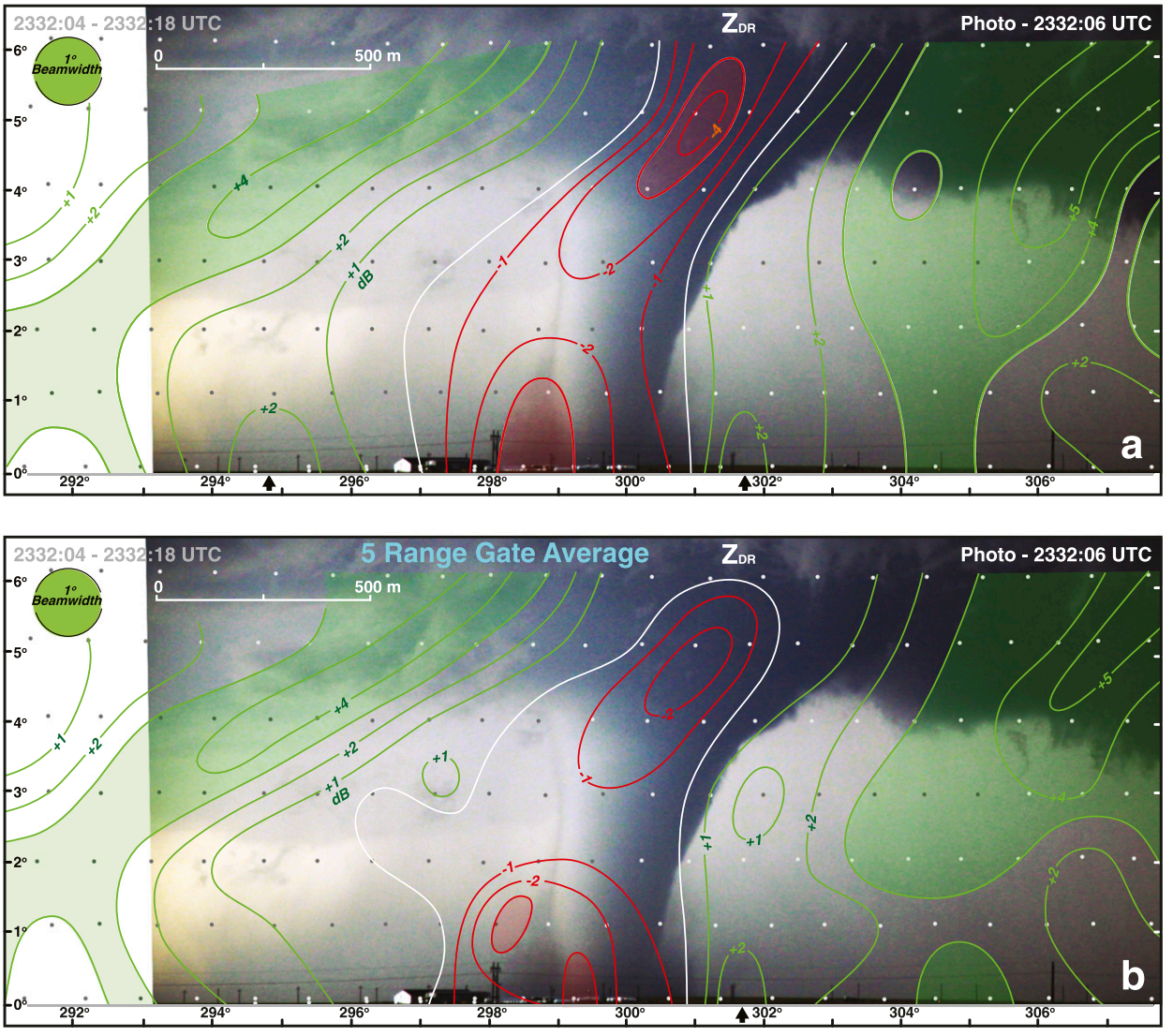

FIG. A2. Photograph of Dodge City tornado 4 at 2332:06 UTC. Radar volume scan is 2332:04–2332:18 UTC. (a) Differential reflectivity Z_{DR}. The same cross section was presented in Fig. 13e. (b) Differential reflectivity averaged over five range gates. Red and green lines are isopleths of negative and positive Z_{DR}, respectively; $Z_{DR} > 3$ dB and < -3 dB are shaded green and red, respectively. Black arrows in (a) and (b) denote low-level regions of high Z_{DR}. The green circle represents the 1° beamwidth of the radar. The scales labeled in the figures are valid at the distance to the center of the tornado. The small dots represent the raw data points from RaXPol.

A summary of the observations presented in this study are shown in the schematic models (Fig. 21). The areas of high debris loading at low levels during the early stages on the tornado's life cycle and after the debris cloud envelops the funnel cloud are shown in the figure. The band of high radar reflectivity that connects the hook echo with the main body of the storm and is associated primarily with hydrometeors is shown to the left (south) of the tornado. Small debris lofted by strong winds flowing into the weak echo notch of the hook echo is outlined in Fig. 21a. The areas of common debris alignment, illustrated as vertically oriented wheat stems among other lofted debris, are highlighted in both schematics. Hydrometeors within the mature tornado are shown (Fig. 21b). These hydrometeors result in a column of positive Z_{DR} and may be masking the vertical debris alignment of the small particles. Bodine et al. (2014) created a schematic of the polarimetric TDS as a function of height (see their Fig. 12). The results shown in this paper, however, suggest a more complex relationship between the radar reflectivity and ρ_{hv}.

The current study has illuminated the complex relationship between lofted debris and the accompanying debris cloud with the TDS signature commonly

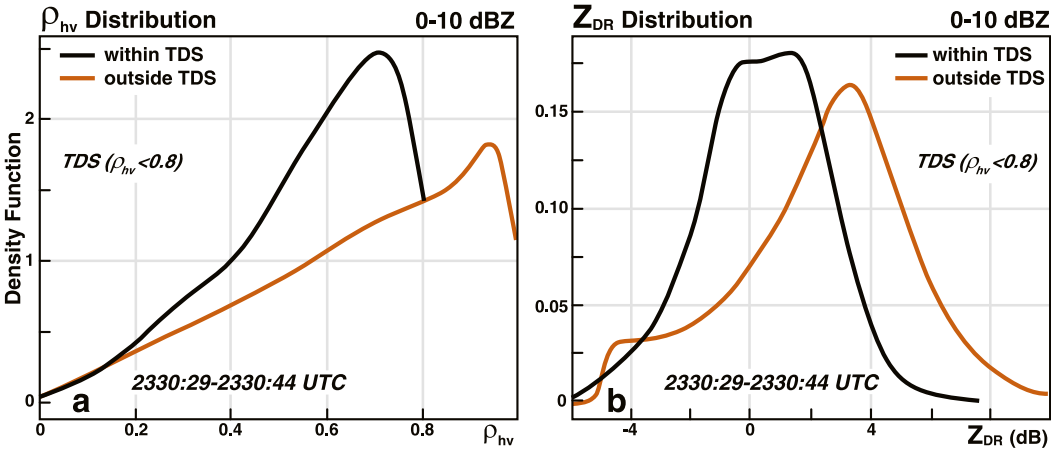

FIG. A3. Distribution plots for the 2330:29–2330:44 UTC volume scan of (a) ρ_{hv} and (b) Z_{DR} within (black lines) and outside (brown lines) of the TDS for radar reflectivities between 0 and 10 dBZ.

observed using polarimetric radars. The continued expansion of the debris cloud as the tornado weakens and the funnel cloud narrows will be a focus of future analyses. In addition, there is an opportunity to perform a similar photogrammetric analysis on tornado 1 (Fig. 5) to determine if the polarimetric features described in this paper are replicated. Future studies of simulated lofted debris are encouraged in order to verify the existence of vertically oriented particles that have been hypothesized in the current study.

Acknowledgments. Zach Wienhoff, Howard Bluestein, and Dylan Reif were supported by NSF Grant AGS-1560945. Roger Wakimoto was supported by NSF's Independent and Research/Development (IRD) program. RaXPol was acquired with MRI funding from NSF Grant AGS-0821231. John Meier, Tian You, and Bob Palmer at the Advanced Radar Research Center (ARRC) at the University of Oklahoma supported RaXPol field operations. The comments from David Bodine and two anonymous reviewers greatly improved an earlier version of this manuscript. Discussions with Jasper Kok are also greatly appreciated.

APPENDIX

Spatial Variability of the Polarimetric Variables

Polarimetric radar measurements are prone to errors as ρ_{hv} decreases, especially in regions of low signal-to-noise ratio such as within the WEC. Accordingly, it is possible that slight shifts in the location of the cross section in range could change the analyses shown in this paper. Outlier data points could also have a large impact on the ρ_{hv} and Z_{DR} fields. One approach to address these concerns is to range average ρ_{hv} and Z_{DR} and replot the cross sections. Several cross sections were chosen and a five-range gate average (i.e., an average over a radial distance of 75 m) was performed and new vertical cross sections were constructed.

Examples of the reanalysis for 2332:06 UTC are presented in Figs. A1 and A2. The original plots shown in Figs. 13d and 13e are also included in the figures. As expected, both the ρ_{hv} and Z_{DR} profiles that have been averaged exhibit reduced minima and maxima when compared with the original vertical cross sections. However, the general patterns of ρ_{hv} and Z_{DR} have not been altered significantly and the main conclusions stated in the manuscript would not have changed. Indeed, the black arrows that denote regions of low ρ_{hv} at low levels in the original cross section (Fig. A1a) are still apparent in Fig. A1b. One of the small areas of high Z_{DR} at low levels shown in Fig. A2a (black arrow located in ~295°) is no longer present in Fig. A2b, but the other region of high Z_{DR} near ~302° is still apparent. The former was not a major contributor to the conclusions presented in the current study.

It is also possible that low ρ_{hv} and Z_{DR} in regions of low radar reflectivity are an artifact of the low signal-to-noise ratio in the TDS. Distribution plots of ρ_{hv} and Z_{DR} were produced in the both the TDS and non-TDS regions for radar reflectivities between 0 and 10 dBZ to determine if there was a systematic difference between these two plots. The TDS was defined as $\rho_{hv} < 0.8$ within the rotational couplet. The ρ_{hv} and Z_{DR} data were binned for a number of different radar volume scans. All of the distribution plots produced similar results even when the data were further partitioned into two separate distributions for radar reflectivities between 0–5 and 5–10 dBZ.

An example of the distribution plots for the 2330:29–2330:44 UTC volume scan is shown in Fig. A3. The ρ_{hv} and Z_{DR} distributions are different when comparing the plots within and outside of the TDS. The maximum in ρ_{hv} is lower (~0.7) for the TDS region owing to the presence of lofted debris when compared to the non-TDS region (Fig. A3a). The maximum in Z_{DR} also occurs near 0 within the TDS versus the corresponding positive peak outside of the TDS (Fig. A3b). Moreover, the former exhibits a bimodal distribution with two maxima that are associated with positive and negative Z_{DR}. The latter peak represents the negative Z_{DR} column discussed in section 3 while the former results from the positive Z_{DR} outside of this column but still within the TDS. The positive maximum in Z_{DR} outside of the TDS suggests the presence of hydrometeors.

REFERENCES

Abrams, T., 1952: *The Manual of Photogrammetry*. George Banta Publishing, 876 pp.

Bluestein, H. B., 1986: Visual aspects of the flanking line in severe thunderstorms. *Mon. Wea. Rev.*, **114**, 788–795, https://doi.org/10.1175/1520-0493(1986)114<0788:VAOTFL>2.0.CO;2.

——, C. C. Weiss, and A. L. Pazmany, 2004: The vertical structure of a tornado near Happy, Texas, on 5 May 2002: High-resolution, mobile, W-band, Doppler radar observations. *Mon. Wea. Rev.*, **132**, 2325–2337, https://doi.org/10.1175/1520-0493(2004)132<2325:TVSOAT>2.0.CO;2.

——, ——, M. M. French, E. M. Holthaus, and R. L. Tanamachi, 2007a: The structure of tornadoes near Attica, Kansas, on 12 May 2004: High-resolution, mobile, Doppler radar observations. *Mon. Wea. Rev.*, **135**, 475–506, https://doi.org/10.1175/MWR3295.1.

——, M. M. French, R. L. Tanamachi, S. Frasier, K. Hardwick, F. Junyent, and A. L. Pazmany, 2007b: Close-range observations of tornadoes in supercells made with dual-polarization, X-band, mobile, Doppler radar. *Mon. Wea. Rev.*, **135**, 1522–1543, https://doi.org/10.1175/MWR3349.1.

——, J. C. Snyder, and J. B. Houser, 2015: A multiscale overview of the El Reno, Oklahoma, tornadic supercell of 31 May 2013. *Wea. Forecasting*, **30**, 525–552, https://doi.org/10.1175/WAF-D-14-00152.1.

Bodine, D. J., M. R. Kumjian, R. D. Palmer, P. L. Heinselman, and A. V. Ryzhkov, 2013: Tornado damage estimation using polarimetric radar. *Wea. Forecasting*, **28**, 139–158, https://doi.org/10.1175/WAF-D-11-00158.1.

——, R. D. Palmer, and G. Zhang, 2014: Dual-wavelength polarimetric radar analyses of tornadic debris signatures. *J. Appl. Meteor. Climatol.*, **53**, 242–261, https://doi.org/10.1175/JAMC-D-13-0189.1.

——, ——, T. Maruyama, C. J. Fulton, Y. Zhu, and B. L. Cheong, 2016a: Simulated frequency dependence of radar observations of tornadoes. *J. Atmos. Oceanic Technol.*, **33**, 1825–1842, https://doi.org/10.1175/JTECH-D-15-0120.1.

——, T. Maruyama, R. D. Palmer, C. J. Fulton, H. B. Bluestein, and D. C. Lewellen, 2016b: Sensitivity of tornado dynamics to soil debris loading. *J. Atmos. Sci.*, **73**, 2783–2801, https://doi.org/10.1175/JAS-D-15-0188.1.

Cheong, B. L., D. J. Bodine, C. J. Fulton, S. M. Torres, T. Maruyama, and R. D. Palmer, 2017: SimRadar: A polarimetric radar time series simulator for tornadic debris studies. *IEEE Trans. Geosci. Remote Sens.*, **55**, 2858–2870, https://doi.org/10.1109/TGRS.2017.2655363.

Doswell, C. A., and H. E. Brooks, 2002: Lessons learned from the damage produced by the tornadoes of 3 May 1999. *Wea. Forecasting*, **17**, 611–618, https://doi.org/10.1175/1520-0434(2002)017<0611:LLFTDP>2.0.CO;2.

Dowell, D. C., C. R. Alexander, J. M. Wurman, and L. J. Wicker, 2005: Centrifuging of hydrometeors and debris in tornadoes: Radar-reflectivity patterns and wind-measurement errors. *Mon. Wea. Rev.*, **133**, 1501–1524, https://doi.org/10.1175/MWR2934.1.

Fujita, T. T., 1981: Tornadoes and downbursts in the context of generalized planetary scales. *J. Atmos. Sci.*, **38**, 1511–1534, https://doi.org/10.1175/1520-0469(1981)038<1511:TADITC>2.0.CO;2.

Griffin, C. B., D. J. Bodine, and R. D. Palmer, 2017: Kinematic and polarimetric radar observations of the 10 May 2010, Moore–Choctow, Oklahoma, tornadic debris signature. *Mon. Wea. Rev.*, **145**, 2723–2741, https://doi.org/10.1175/MWR-D-16-0344.1.

Hildebrand, P. H., and R. K. Moore, 1990: Meteorological radar observations from mobile platforms. *Radar in Meteorology,* D. Atlas, Ed., Amer. Meteor. Soc., 287–314.

Holle, R. L., 1986: Photogrammetry of thunderstorms. *Thunderstorms: A Social and Technological Documentary*, 2nd ed. E. Kessler, Ed., Vol. 3, University of Oklahoma, 77–98.

Houser, J. L., H. B. Bluestein, and J. C. Snyder, 2016: A finescale radar examination of the tornadic debris signature and weak-echo reflectivity band associated with a large, violent tornado. *Mon. Wea. Rev.*, **144**, 4101–4130, https://doi.org/10.1175/MWR-D-15-0408.1.

Kandler, K., and Coauthors, 2007: Chemical composition and complex refractivity index of Saharan mineral dust at Izaña, Tenerife (Spain) derived by electron microscopy. *Atmos. Environ.*, **41**, 8058–8074, https://doi.org/10.1016/j.atmosenv.2007.06.047.

Kosiba, K., and J. Wurman, 2010: The three-dimensional axisymmetric wind field structure of the Spencer, South Dakota, 1998 tornado. *J. Atmos. Sci.*, **67**, 3074–3083, https://doi.org/10.1175/2010JAS3416.1.

——, and ——, 2013: The three-dimensional structure and evolution of a tornado boundary layer. *Wea. Forecasting*, **28**, 1552–1561, https://doi.org/10.1175/WAF-D-13-00070.1.

——, R. J. Trapp, and J. Wurman, 2008: An analysis of the axisymmetric three-dimensional low level wind field in a tornado using mobile radar observations. *Geophys. Res. Lett.*, **35**, L05805, https://doi.org/10.1029/2007GL031851.

Kumjian, M. R., and A. V. Ryzhkov, 2008: Polarimetric signatures in supercell thunderstorms. *J. Appl. Meteor. Climatol.*, **47**, 1940–1961, https://doi.org/10.1175/2007JAMC1874.1.

——, and ——, 2009: Storm-relative helicity revealed from polarimetric radar measurements. *J. Atmos. Sci.*, **66**, 667–685, https://doi.org/10.1175/2008JAS2815.1.

Kurdzo, J. M., D. J. Bodine, B. L. Cheong, and R. D. Palmer, 2015: High-temporal resolution polarimetric X-band Doppler radar observations of the 20 May 2013 Moore, Oklahoma, tornado. *Mon. Wea. Rev.*, **143**, 2711–2735, https://doi.org/10.1175/MWR-D-14-00357.1.

——, and Coauthors, 2017: Observations of severe local storms and tornadoes with the atmospheric imaging radar. *Bull. Amer. Meteor. Soc.*, **98**, 915–935, https://doi.org/10.1175/BAMS-D-15-00266.1.

Lee, W.-C., and J. Wurman, 2005: Diagnosed three-dimensional axisymmetric structure of the Mulhall tornado on 3 May 1999. *J. Atmos. Sci.*, **62**, 2373–2393, https://doi.org/10.1175/JAS3489.1.

Lewellen, D. C., B. Gong, and W. S. Lewellen, 2008: Effects of finescale debris on near-surface tornado dynamics. *J. Atmos. Sci.*, **65**, 3247–3262, https://doi.org/10.1175/2008JAS2686.1.

Malkus, J., 1952: The slopes of cumulus clouds in relation to external wind shear. *Quart. J. Roy. Meteor. Soc.*, **78**, 530–542, https://doi.org/10.1002/qj.49707833804.

Nolan, D. S., 2013: On the use of Doppler radar-derived wind fields to diagnose the secondary circulations of tornadoes. *J. Atmos. Sci.*, **70**, 1160–1171, https://doi.org/10.1175/JAS-D-12-0200.1.

Okada, K., J. Heintzenberg, K. Kai, and Y. Qin, 2001: Shape of atmospheric mineral particles collected in three Chinese arid regions. *Geophys. Res. Lett.*, **28**, 3123–3126, https://doi.org/10.1029/2000GL012798.

Pazmany, A. L., J. B. Mead, H. B. Bluestein, J. C. Snyder, and J. B. Houser, 2013: A mobile rapid-scanning X-band polarimetric (RaXPol) Doppler radar system. *J. Atmos. Oceanic Technol.*, **30**, 1398–1413, https://doi.org/10.1175/JTECH-D-12-00166.1.

Ryzhkov, A., T. Schuur, D. W. Burgess, and D. S. Zrnić, 2005: Polarimetric tornado detection. *J. Appl. Meteor.*, **44**, 557–570, https://doi.org/10.1175/JAM2235.1.

Saari, M. D. W., R. M. Lawton, C. J. Schultz, and L. D. Carey, 2014: Early characteristics of the polarimetric tornadic debris signature associated with the 20 May 2013 Newcastle–Moore, Oklahoma tornado. *J. Oper. Meteor.*, **2**, 110–114, https://doi.org/10.15191/nwajom.2014.0210.

Schultz, C. J., and Coauthors, 2012a: Dual-polarization tornadic debris signatures. Part I: Examples and utility in an operational setting. *Electron. J. Oper. Meteor.*, **13**, 120–137.

——, and Coauthors, 2012b: Dual-polarization tornadic debris signatures. Part II: Comparison and caveats. *Electron. J. Oper. Meteor.*, **13**, 138–150.

Snyder, J. C., and H. B. Bluestein, 2014: Some considerations for the use of high-resolution mobile radar data in tornado intensity determination. *Wea. Forecasting*, **29**, 799–827, https://doi.org/10.1175/WAF-D-14-00026.1.

Tanamachi, R. L., H. B. Bluestein, W.-C. Lee, M. Bell, and A. Pazmany, 2007: Ground-based velocity track display (GBVTD) analysis of W-band Doppler radar data in a tornado near Stockton, Kansas, on 15 May 1999. *Mon. Wea. Rev.*, **135**, 783–800, https://doi.org/10.1175/MWR3325.1.

——, ——, J. B. Houser, S. J. Frasier, and K. M. Hardwick, 2012: Mobile, X-band, polarimetric Doppler radar observations of the 4 May 2007 Greensburg, Kansas, tornadic supercell. *Mon. Wea. Rev.*, **140**, 2103–2125, https://doi.org/10.1175/MWR-D-11-00142.1.

Umeyama, A., B. L. Cheong, S. Torres, and D. Bodine, 2018: Orientation analysis of simulated tornadic debris. *J. Atmos. Oceanic Technol.*, **35**, 993–1010, https://doi.org/10.1175/JTECH-D-17-0140.1.

Van Den Broeke, M. S., 2015: Polarimetric tornadic debris signature variability and debris fallout signatures. *J. Appl. Meteor. Climatol.*, **54**, 2389–2405, https://doi.org/10.1175/JAMC-D-15-0077.1.

——, and S. T. Jauernic, 2014: Spatial and temporal characteristics of polarimetric tornadic debris signatures. *J. Appl. Meteor. Climatol.*, **53**, 2217–2231, https://doi.org/10.1175/JAMC-D-14-0094.1.

Wakimoto, R. M., and B. E. Martner, 1992: Observations of a Colorado tornado. Part II: Combined photogrammetric and Doppler radar analysis. *Mon. Wea. Rev.*, **120**, 522–543, https://doi.org/10.1175/1520-0493(1992)120<0522:OOACTP>2.0.CO;2.

——, W.-C. Lee, H. B. Bluestein, C.-H. Liu, and P. H. Hildebrand, 1996: ELDORA observations during VORTEX 95. *Bull. Amer. Meteor. Soc.*, **77**, 1465–1481, https://doi.org/10.1175/1520-0477(1996)077<1465:EODV>2.0.CO;2.

——, N. T. Atkins, and J. Wurman, 2011: The LaGrange tornado during VORTEX2. Part I: Photogrammetric analysis of the tornado combined with single-Doppler radar data. *Mon. Wea. Rev.*, **139**, 2233–2258, https://doi.org/10.1175/2010MWR3568.1.

——, P. Stauffer, and W.-C. Lee, 2012: Finescale structure of the LaGrange, Wyoming, tornado during VORTEX2: GBVTD and photogrammetric analysis. *Mon. Wea. Rev.*, **140**, 3397–3418, https://doi.org/10.1175/MWR-D-12-00036.1.

——, N. T. Atkins, K. M. Butler, H. B. Bluestein, K. Thiem, J. Snyder, and J. Houser, 2015: Photogrammetric analysis of the 2013 El Reno tornado combined with mobile X-band polarimetric radar data. *Mon. Wea. Rev.*, **143**, 2657–2683, https://doi.org/10.1175/MWR-D-15-0034.1.

——, and Coauthors, 2016: Aerial damage survey of the 2013 El Reno tornado combined with mobile radar data. *Mon. Wea. Rev.*, **144**, 1749–1776, https://doi.org/10.1175/MWR-D-15-0367.1.

Wienhoff, Z. B., H. B. Bluestein, L. J. Wicker, J. C. Snyder, A. Shapiro, C. K. Potvin, J. B. Houser, and D. W. Reif, 2018: Applications of a spatially variable advection correction technique for temporal correction of dual-Doppler analyses of tornadic supercells. *Mon. Wea. Rev.*, **146**, 2949–2971, https://doi.org/10.1175/MWR-D-17-0360.1.

Wurman, J., 2002: The multiple-vortex structure of a tornado. *Wea. Forecasting*, **17**, 473–505, https://doi.org/10.1175/1520-0434(2002)017<0473:TMVSOA>2.0.CO;2.

——, and S. Gill, 2000: Finescale radar observations of the Dimmitt, Texas (2 June 1995), tornado. *Mon. Wea. Rev.*, **128**, 2135–2164, https://doi.org/10.1175/1520-0493(2000)128<2135:FROOTD>2.0.CO;2.

——, and K. Kosiba, 2013: Finescale radar observations of tornado and mesocyclone structures. *Wea. Forecasting*, **28**, 1157–1174, https://doi.org/10.1175/WAF-D-12-00127.1.

——, J. M. Straka, and E. N. Rasmussen, 1996: Fine-scale Doppler radar observations of tornadoes. *Science*, **272**, 1774–1777, https://doi.org/10.1126/science.272.5269.1774.

——, C. Alexander, P. Robinson, and Y. Richardson, 2007: Low-level winds in tornadoes and potential catastrophic tornado impacts in urban areas. *Bull. Amer. Meteor. Soc.*, **88**, 31–46, https://doi.org/10.1175/BAMS-88-1-31.

——, K. Kosiba, and P. Robinson, 2013: In situ, Doppler radar, and video observations of the interior structure of a tornado and the wind–damage relationship. *Bull. Amer. Meteor. Soc.*, **94**, 835–845, https://doi.org/10.1175/BAMS-D-12-00114.1.

——, ——, ——, and T. Marshall, 2014: The role of multiple-vortex tornado structure in causing storm researcher facilities. *Bull. Amer. Meteor. Soc.*, **95**, 31–45, https://doi.org/10.1175/BAMS-D-13-00221.1.

Zehnder, J. A., J. Hu, and A. Razdan, 2007: A stereo photogrammetric technique applied to orographic convection. *Mon. Wea. Rev.*, **135**, 2265–2277, https://doi.org/10.1175/MWR3401.1.